Hydromechanical Modeling of Nonplanar Three-Dimensional Fracture Propagation Using an Iteratively Coupled Approach

Sanbai Li[a], Abbas Firoozabadi[b, *], and Dongxiao Zhang[c,*]

[a] Department of Civil and Environmental Engineering, University of California, Irvine, CA, U.S.A.
[b] Reservoir Engineering Research Institute, Palo Alto, CA, U.S.A.
[c] School of Environmental Science and Engineering, Southern University of Science and Technology, Shenzhen, 518055, P.R. China

Abstract

Accurate numerical modeling of fracture propagation and deflection in porous media is important in the development of geo-resources. To this end, we propose a novel modeling framework to simulate nonplanar three-dimensional (3-D) fracture growth within poroelastic media, using an iteratively coupled approach based on time-/scale-dependent fracture stiffness. In this approach, the propagating fractures are explicitly tracked and fitted at each growth step using triangular elements that are independent of the matrix discretized by hexahedral grids. The finite volume/finite element method (FVFEM) is employed to solve the hydro-mechanical system, based on the embedded discrete fracture model (EDFM). The calculated pressure in fractures and the stress state of the host grid of the embedded fractures constitute the boundary conditions for the boundary element method (BEM). The BEM module, in turn, renders the evolving fracture stiffness and aperture for the FVFEM module. Finally, the total stresses and the fracture-tip displacements are computed at the end of each time step to estimate the velocity and direction of newly created fractures ahead of the fracture tip. The proposed model is first validated against analytical solutions. Then, in three different examples, results are shown from the fracture's footprint under layered stress conditions, simultaneous propagation of two nonplanar 3-D fractures, and the mechanical interaction of en échelon arrays. This work presents an efficient framework to simulate propagation of nonplanar fractures, and establishes the foundation to build an integrated simulator for fracture propagation, proppant transport, and production forecasting in unconventional formations.

Keywords:

fracture propagation; nonplanar 3-D fractures; hydraulic fracturing; growth of en échelon arrays; 3-D BEM.

*Corresponding author
E-mail addresses: af@rerinst.org (A. Firoozabadi), zhangdx@sustech.edu.cn (D. Zhang)

Key Points:

- A model for propagation of complex 3-D nonplanar fractures is proposed and verified
- An iteratively coupled approach is proposed based on time-/scale-dependent fracture stiffness
- Propagation of 3-D en échelon arrays is investigated under the stress shadowing effect

1. Introduction

Prediction of fracture propagation and deflection in geological materials is important to many subsurface engineering problems, such as hydraulic fracturing in oil/gas/geothermal reservoirs, disposal of high-level nuclear waste, geological sequestration of CO_2, and underground storage of oil/gas/compressed air energy. The development of shale oil/gas formations with ultra-low permeability relies on massive hydraulic fracturing for creating fractures to enhance the formations permeability and connectivity. Hydraulic fracturing facilitates the extraction of heat energy from hot dry rock formations, in which the hydraulically created fractures serve as high-conductivity passages and significant sites for heat exchange to maintain a high flow rate at high temperatures [*Li et al.*, 2019]. It is highly desirable to create extensive fracture networks in heat extraction in geo-resource formations [*Cipolla et al.*, 2010; *Izadi and Elsworth*, 2014; *Li and Zhang*, 2018]. On the other end of the spectrum, underground storage projects require prevention of fracturing in the caprock, or at least a slowing down of fracture propagation for guaranteeing the integrity of the storage site from a long-term perspective. Knowledge regarding the scale, geometry, and complexity of hydraulically-created fractures is crucial in geo-resource and subsurface storage formations. A critical need exists to develop physics-based numerical models to predict fracture growth with multi-scale, multi-dimensional, and multi-physics characteristics, to gain better insights into various complex phenomena [*Paul et al.*, 2018].

A vast literature exists on modeling of fracture propagation in subsurface rock. The numerical methods include the Finite Element Method (FEM), the Boundary Element Method (BEM), and the Discrete Element Method (DEM). Traditional FEM may not properly simulate fracture growth because it may not describe fracture geometry, fracture aperture, and fluid pressure in the fractures. Many extensions of the FEM have been introduced to alleviate this deficiency. These include node-splitting FEM [*Ji et al.*, 2009; *Kim and Moridis*, 2015], Generalized FEM (GFEM) [*Duarte et al.*, 2001; *Duarte et al.*, 2007; *Gupta and Duarte*, 2018; *Gupta et al.*, 2012; *Pereira et al.*, 2009], and eXtended FEM (XFEM) [*Belytschko and Black*, 1999; *Gordeliy and Peirce*, 2013; 2015; *Moës et al.*, 1999; *Mohammadnejad and Andrade*, 2016].

Node-splitting FEM follows the physical process of fracture opening when the effective stresses satisfy a tensile failure criterion [*Kim and Moridis*, 2015]. Because the fracture growth path must be aligned with the boundary of the pre-existing elements, there is a problem in simulating the growth of complex nonplanar 3-D fractures with fitted geometries. Both GFEM and XFEM are based on the partition of unity methods, in which enrichment functions are specifically designed for representing discontinuity displacements across the fracture surfaces and the singular stresses at the fracture tips. Most of these models have deficiency in describing fracture brunching and coalescing due to substantial inaccuracy in numerical implementations, and therefore are often limited to a simple fracture topology [*Dittmann et al.*, 2019]. Recently, *Gupta and Duarte* [2018] proposed an improved GFEM, featured as explicit fracture surface representations with adaptive mesh refinement. However, this model does not include the fluid leakoff from the fracture to the matrix. The model is constrained to predicting toughness-dominated and viscosity-dominated fracture growth. Other propagation regimes, such as storage-dominated, leakoff-dominated, and the intermediate, are beyond this model's capacity. The Phase-Field Method (PFM) [*Lee et al.*, 2016; *Miehe et al.*, 2015; *Permann et al.*, 2016; *Wick et al.*, 2016; *Wilson and Landis*, 2016] accommodates many complexities in the simulation of fracture propagation of fully 3-D in elastic, heterogeneous, and anisotropic rock mass based on multi-physics processes. It also processes shortcomings including use of regularization to make the transition from fracture to matrix smooth. This regularization requires high-resolution meshes in the vicinity of fractures [*Lecampion et al.*, 2018]. The smearing nature of the PFM also creates challenges to reconstruct the fracture aperture and to accurately calculate the leakoff [*Lecampion et al.*, 2018]. The PFM is based on decomposition of the stress tensor into tension and compression. The decomposition may also introduce strong nonlinearities in the numerical solution [*Ambati et al.*, 2015].

In the BEM, the use of Green's function, reduces the dimension of the problem through integration over the boundary. Besides, the BEM has higher accuracy in calculating the fracture aperture and stresses than the FEM and is applicable for predicting fracture propagation with complex topologies. These clear advantages have made the BEM popular in modeling fracture growth in 2-D [*Cheng et al.*, 2020; *Hou et al.*, 2016; *Olson*, 2004], planar 3-D [*Tang et al.*, 2016; *Zhang et al.*, 2017], nonplanar 2.5-D [*Kresse et al.*, 2013; *Weng et al.*, 2011], and nonplanar 3-D geometries [*Castonguay et al.*, 2013; *Cherny et al.*, 2016; *Kumar and Ghassemi*, 2018; *Shen and Shi*, 2019; *Tang et al.*, 2019; *Thomas et al.*, 2020b]. In most of the extant literature, fluid exchange between the matrix and the fracture and fluid flow in the matrix is either simplified or neglected via assuming an impermeable matrix or employing the 1-D leak-off model suggested by *Carter* [1957]. The leakoff can affect hydraulic fracturing, especially for waterless fracturing when the fracturing fluid has low viscosity [*Li and Zhang*, 2019]. Neglect of the seepage of fracturing fluid into the matrix would lead to large errors in prediction of fracture aperture, because the poroelastic effect (e.g., the backstress induced by matrix dilation) is removed from this system [*Salimzadeh et al.*, 2017]. The magnitude of the leakoff is proportional to the pressure difference between the matrix and the fracture. Using a simplified time-dependent leak-off model tends to produce unprecise modeling results [*Salimzadeh et al.*, 2017]. Another broadly used method for fracture growth is the DEM, proposed by *Cundall* [1971]. The DEM is effective in predicting complicated mechanical behaviors, such as branching, merging, kinking, etc. Fracture propagation and fracture intersection during hydraulic fracturing have been investigated in [*Damjanac and Cundall*, 2016; *Hamidi and Mortazavi*, 2014; *Nagel et al.*, 2013; *Yoon et al.*, 2015] based on the DEM. The main challenge of the DEM is to calibrate/update the particles' properties, e.g., grain size, shear and normal stiffnesses of the bond before/during the simulation. The fracture normal stiffness relies not only on the magnitude of the stress that is applied on the fracture, but also on the geometry and scale of the propagating fracture. If the updated normal stiffness is of low accuracy, a larger computational error would result in fracture aperture. The flow rate across the fracture is proportional to the fracture width to the third-power, i.e., $q \propto -w_f^3\, dp/dx$, according to Poiseuille's law [*Brown*, 1987]. Modeling of fracture growth often requires a large number of particles to render acceptable accuracy, which may hinder its application to real field problems.

In this work, a hybrid approach is presented to simulate fracturing that results in nonplanar 3-D fractures. Two independent grid systems are utilized to represent the fracture and the matrix. Hexahedral gridding is used for the fixed matrix throughout the simulation while the dynamic triangular grid system is used for tracking and fitting the extended fracture geometry. The fluid flow through the fracture and the fluid exchange between the fracture and the matrix is described by the embedded discrete fracture model (EDFM). This technique allows leakoff in fully 3-D, circumventing the limitations in Carter's model. Independent fracture representation allows nonplanar 3-D fracture propagation within the surrounding matrix with flexibility. The fracture aperture is accurately estimated through the BEM, with which an equivalent stress intensity factor ahead of the fracture is calculated to describe the fracture's propagation in a mixed mode (i.e., opening, shearing, and tearing). A new iteratively coupled approach is proposed to solve the problem of arbitrary 3-D fracture propagation in poroelastic media, in which the time-/scale-dependent fracture stiffness is evaluated by the BEM via introducing a small perturbation to fluid pressure in the fracture.

The structure of the rest of the paper is as follows. In Section 2, the governing equations to describe fracture propagation are derived. Numerical discretization is introduced in Section 3. Then, the solution strategy and fracture growth criteria are presented in Section 4, followed by validation examples to quantify the viability, accuracy, and applicability of the proposed model (i.e., Section 5). In Section 6, three numerical examples are designed and analyzed. Finally, a brief summary of this work is presented in Section 7.

2. Governing Equations

The major goal is to propose a modeling framework for propagation of nonplanar 3-D fractures in poroelastic media. In this framework, the porous medium domain Ω with boundary $\partial\Omega$ (Figure 1), is assumed to be a homogeneous, isotropic, linear elastic material with infinitesimal strain; the fracture Γ that consists of positive and negative surfaces (i.e., $\Gamma=\Gamma^{+}\cup\Gamma^{-}$), embedded into the porous medium domain Ω, is explicitly treated as an internal boundary subjected to a traction $p_f\boldsymbol{n}_s$ (i.e., Neumann boundary). Based on the poroelasticity theory [*Coussy*, 2004], we derive a set of expressions to describe the fracture propagation in poroelastic media, which includes fluid flow in the rock matrix and the fractures, mechanical deformation of the matrix and the fractures, and fluid-driven fracture propagation.

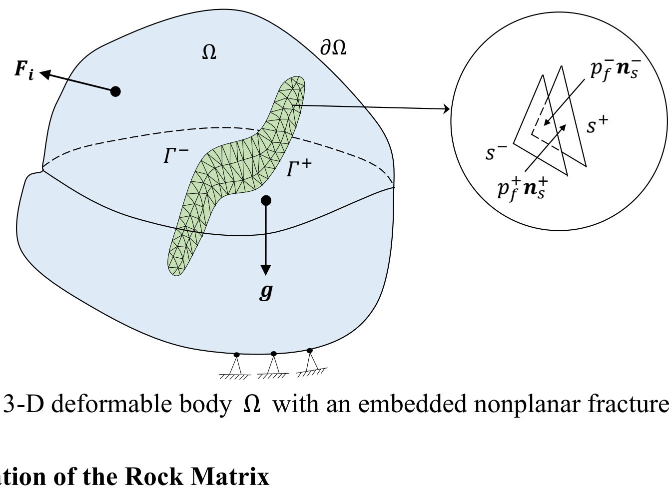

Figure 1. Illustration of a 3-D deformable body Ω with an embedded nonplanar fracture Γ.

2.1 Mechanical Deformation of the Rock Matrix

At quasi-static conditions, the governing equation of geomechanical deformation of rock mass can be expressed as follows：

$$\boldsymbol{\nabla}\cdot\boldsymbol{\sigma}+\rho_b\boldsymbol{g}=\boldsymbol{0} \tag{1}$$

where $\boldsymbol{\sigma}$ is the Cauchy total stress tensor; the symbol '·' denotes a single contraction of adjacent indices of two tensors; $\boldsymbol{g}$ is the gravity vector; $\rho_b=\phi\rho_f+(1-\phi)\rho_s$ is the bulk density; ρ_f is the fluid density; ρ_s is the solid density; and ϕ is the porosity. We employ the convention that tensile stress is positive. The effective stress for a saturated porous rock is defined as:

$$\boldsymbol{\sigma}=\boldsymbol{C_{dr}}:\boldsymbol{\varepsilon}-bp_m\boldsymbol{I} \tag{2}$$

where $b=1-K/K_s$ is the Biot coefficient; K and K_s are the drained bulk modulus and rock skeleton modulus, respectively; p_m is the pore pressure in the matrix; $\boldsymbol{I}$ is the rank-2 identity tensor; $\boldsymbol{C_{dr}}$ is the rank-4 drained elasticity tensor; the symbol ':' denotes a double contraction of adjacent indices of a tensor of rank two or higher; and $\boldsymbol{\varepsilon}$ is the linearized strain tensor under the assumption of infinitesimal transformation:

$$\boldsymbol{\varepsilon}=\frac{1}{2}(\boldsymbol{\nabla}\otimes\boldsymbol{u}+\boldsymbol{u}\otimes\boldsymbol{\nabla}) \tag{3}$$

where $\boldsymbol{u}$ is the displacement vector; and the symbol '⊗' denotes a juxtaposition of two vectors. Taking the embedded fracture into account (see Figure 1), one needs to add the surface tractions, induced by hydraulic loading and/or surface contact stress,

$$\boldsymbol{t}_\Gamma=p_f\boldsymbol{n}_s+\boldsymbol{\sigma}_t\cdot\boldsymbol{n}_s \tag{4}$$

into the momentum balance equation, where p_f is the fluid pressure in the fracture; $\boldsymbol{n}$ is the outward unit normal vector of the fracture surface Γ; $\boldsymbol{\sigma}_t$ is the contact stress related to the closed rough fractures ($\boldsymbol{\sigma}_t=\boldsymbol{0}$ for open fractures); and the subscripts s and N are the fracture surface and the number of imbedded fractures, respectively. Submitting Eqs. (2) to (4) into Eq. (1), we may obtain a comprehensive momentum balance equation for a saturated rock system with embedded fractures:

$$\begin{gathered}\iiint_\Omega\left[\boldsymbol{\nabla}\cdot\left(\frac{1}{2}\boldsymbol{C_{dr}}:(\boldsymbol{\nabla}\otimes\boldsymbol{u}+\boldsymbol{u}\otimes\boldsymbol{\nabla})-bp_m\boldsymbol{I}\right)+\rho_b\boldsymbol{g}\right]d\Omega\\-\sum_{i=1}^{N}\left[\oiint_{\Gamma_i}(p_f\boldsymbol{n}_s+\boldsymbol{\sigma}_t\cdot\boldsymbol{n}_s)ds\right]=\boldsymbol{0}\end{gathered} \tag{5}$$

2.2 Fluid Flow in the Matrix

Based on the concept of continuum representation, i.e., the fluid and solid occupy an overlapping space, the governing equation for mass balance of single-phase flow can be uniformly expressed as follows:

$$\frac{dm}{dt}+\boldsymbol{\nabla}\cdot\boldsymbol{F}+Q_L=Q_{sm} \tag{6}$$

where m denotes the fluid mass; t is the time; Q_L is the leak-off term; Q_{sm} is a source term in the matrix; and $\boldsymbol{F}$ is the flux term. The constitutive relations for coupled single-phase flow and elastic geomechanics are written as [*Coussy*, 2004]:

$$\delta m = \rho_f \left(b\delta\epsilon + \frac{\delta p_m}{M} \right) \tag{7}$$

$$\frac{1}{M} = \frac{\phi}{K_f} + \frac{b-\phi}{K_s} \tag{8}$$

where $\epsilon = \boldsymbol{\nabla} \cdot \boldsymbol{u}$ is the volumetric strain; M is the Biot modulus; and K_f is the fluid modulus. According to Darcy's law, the fluid flux term may be expressed as:

$$\boldsymbol{F} = \rho_f \boldsymbol{v}_m = -\frac{\rho_f}{\mu} \boldsymbol{k}_m \cdot (\boldsymbol{\nabla} p_m - \rho_f \boldsymbol{g}) \tag{9}$$

where μ is the fluid viscosity and $\boldsymbol{k}_m$ is the absolute permeability tensor of the matrix. The leak-off term Q_L is of great significance to fluid-driven fracture propagation since it represents the fluid exchange between the created fractures and the rock matrix, which may be given as:

$$Q_L = -\rho_f \frac{k_m}{\mu} \frac{\partial (p_f - p_m)}{\partial \boldsymbol{n}_s} \tag{10}$$

Submitting Eqs. (7) through (10) into Eq. (6), we obtain comprehensive mass balance equations for the matrix:

$$\begin{gathered} \iiint_{\Omega} \left[\rho_f \left(b \frac{\partial (\boldsymbol{\nabla} \cdot \boldsymbol{u})}{\partial t} + \frac{1}{M} \frac{\partial p_m}{\partial t} \right) \right] d\Omega + \iiint_{\Omega} \left[\boldsymbol{\nabla} \cdot \left(-\frac{\rho_f \boldsymbol{k}_m}{\mu} \cdot (\boldsymbol{\nabla} p_m - \rho_f \boldsymbol{g}) \right) \right] d\Omega \\ - \oiint_{\Gamma} \left(\rho_f \frac{k_m}{\mu} \frac{\partial (p_f - p_m)}{\partial \boldsymbol{n_s}} \right) ds = \iiint_{\Omega} Q_{sm} d\Omega \end{gathered} \tag{11}$$

2.3 Fluid Flow through the Fractures

The governing equations for fluid flow through the fractures are similar to those for fluid in the matrix. In our work we allow fractures to be deformable and assume that they are saturated with a compressible fluid. The mass balance equation in the fractures can be expressed as:

$$\frac{\partial (\rho_f w_f)}{\partial t} + \boldsymbol{\nabla} \cdot (\rho_f w_f \boldsymbol{v}_f) - Q_L = Q_{sf} \tag{12}$$

where w_f is the fracture aperture; Q_{sf} is a source term in the fracture; and $\boldsymbol{v}_f$ is the average velocity of the fluid across a fracture, which may be written, based on cubic law, as:

$$\boldsymbol{v}_f = \frac{w_f^2 \boldsymbol{I}}{12\mu} \cdot (\boldsymbol{\nabla} p_f - \rho_f \mathbf{g}) \tag{13}$$

The accumulation term, associated with compressible fluid flow through ae deformable fracture, can be expressed as:

$$\frac{\partial(\rho_f w_f)}{\partial t} = \rho_f \frac{\partial w_f}{\partial t} + \frac{w_f \rho_f}{K_f}\frac{\partial p_f}{\partial t} \tag{14}$$

The $\partial w_f/\partial t$ serves as a coupling term that links the poroelastic module and the fluid-driven fracture growth module together. To illustrate how these two modules are coupled, we define the fracture stiffness K_n for the closed and open fractures, respectively, as:

$$K_n = \begin{cases} \partial\sigma_n'/\partial w_f\text{, closed} \\ \partial p_f/\partial w_f\text{, open} \end{cases} \tag{15}$$

where σ_n' is the normal effective stress. For closed fractures, the fracture stiffness is dependent on the normal effective stress and the asperity properties on the fracture surface (i.e., the joint-roughness coefficient (JRC), and the joint-compressive strength (JCS)). Under this circumstance, we explicitly update the fracture aperture change using the Bandis-Barton model as [*Bandis et al.*, 1983]:

$$\frac{\partial w_f}{\partial t} = \left(\frac{1}{v_m} - \frac{K_{ni}}{\partial\sigma_n'/\partial t}\right)^{-1} \tag{16}$$

$$K_{ni} = -7.15 + 1.75JRC + \frac{JCS}{JRC} \tag{17}$$

$$v_m = -0.1023 - 0.0074JRC + 0.4252\left(\frac{JCS}{JRC}\right)^{-0.2510} \tag{18}$$

where K_{ni} is the initial normal stiffness and v_m is the allowed maximum closure. When the fracture is open, driven by high fluid pressure, its stiffness can be related to the fracture fluid pressure. The magnitude of the fracture opening may depend on the matrix deformation surrounding the fracture under hydraulic loading on the fracture surfaces, and that the displacement at an arbitrary point is closely related to hydraulic loading that is applied on another arbitrary point according to Kelvin's solution [*Sokolnikoff and Specht*, 1956]. As a result, the stiffness of an open fracture is a function of fluid pressure within the fracture, mechanical properties of the matrix (i.e., Young's modulus and Poisson's ratio), and the geometry of the fracture (i.e., the fracture shape and size). Since an analytical solution for variable fracture stiffness K_n with multiple nonplanar 3-D fractures is not available, we resort to a numerical method, i.e., the three-dimensional displacement discontinuity method (3-D DDM) [*Crouch et al.*, 1983; *Fan et al.*, 2020], which implicitly provides the stiffness. The DDM belongs to an indirect BEM that solves displacement discontinuities on the boundary with prescribed boundary stresses. Details of using 3-D DDM to obtain the fracture stiffness will be introduced in Section 4.2. Here, we only give here the fracture aperture change for open fractures for an implicit fracture stiffness with respect to the fluid pressure as:

$$\frac{\partial w_f}{\partial t} = \frac{1}{K_n}\frac{\partial p_f}{\partial t} \tag{19}$$

By submission of Eqs. (10), (13), (14), and (19) into Eq. (12), we derive the mass balance equation for the fracture as:

$$\iiint_{\Omega_\Gamma}\left[\rho_f\left(\frac{1}{K_n}\frac{\partial p_f}{\partial t}+\frac{w_f}{K_f}\frac{\partial p_f}{\partial t}\right)\right]d\Omega+\iiint_{\Omega_\Gamma}\left[\boldsymbol{\nabla}\cdot\left(-\frac{\rho_f w_f^3\boldsymbol{I}}{12\mu}\cdot(\boldsymbol{\nabla}p_f-\rho\boldsymbol{g})\right)\right]d\Omega \\ +\oiint_{\Gamma}\left(\rho_f\frac{k_m}{\mu}\frac{\partial(p_f-p_m)}{\partial\boldsymbol{n_s}}\right)ds=\iiint_{\Omega_\Gamma}Q_{sf}d\Omega \tag{20}$$

where Ω_Γ is the space domain of the fracture.

3. Spatial and Temporal Discretization

In this work, we use the backward first-order method for time discretization and the fractured media is discretized as two independent computation domains, i.e., the matrix and the fractures. The matrix is divided into a finite number of non-overlapping hexahedral grids. The fracture is partitioned into a series of triangular grids to describe the nonplanar fracture geometry created in propagation.

3.1 Discretization for the Poroelastic System

By introducing interpolation functions for the pressures in the matrix and the fractures and displacement for the matrix, we write:

$$p_m=\sum_{i=1}^{n_{m,ele}}\varphi_i\,p_i;\;\;p_f=\sum_{j=1}^{n_{f,ele}}\varphi_j\,p_j;\;\boldsymbol{u}_m=\sum_{a=1}^{n_{node}}\psi_a\,\boldsymbol{u}_a \tag{21}$$

where n_{node} is the number of nodes of the matrix elements; $n_{m/f,ele}$ is the number of elements of the rock matrix/fracture, respectively; $p_{m/f}$ is the pore pressures of the matrix/fracture, repectively; and $\boldsymbol{u}_a$ is the displacement at the element nodes (vertices) of the matrix. The displacement interpolation functions ψ_a are the usual finite element hat functions, which take a value of 1 at node a, and 0 at all other nodes. φ_i is the pressure interpolation functions of the matrix/fracture. Note that the pressure interpolation functions are discontinuous functions that take the value of 1 at element i, and 0 at all the other elements. We employ the FVFEM to discretize the controlling equations via submitting the above test functions into Eqs. (5), (11), and (20), leading to their weak form. After manipulations, the governing equations are formatted as the required formulations of the Newton-Raphson iterating method, i.e., the residual form:

$$\underbrace{\begin{bmatrix}\boldsymbol{K}_{ab} & -(\boldsymbol{L}_{ia}^{p_m\boldsymbol{u}_m})' & \boldsymbol{0}\\ \boldsymbol{L}_{ib}^{p_m\boldsymbol{u}_m} & \boldsymbol{E}_{ij}^{p_mp_m}+\Delta t\boldsymbol{P}_{ij}^{p_mp_m} & -\left(\boldsymbol{S}_{ij}^{p_fp_m}\right)'\\ \boldsymbol{0} & \boldsymbol{S}_{ij}^{p_fp_m} & \boldsymbol{G}_{ij}^{p_fp_f}+\Delta t\boldsymbol{U}_{ij}^{p_fp_f}\end{bmatrix}^{n+1,k}}_{\boldsymbol{J}}\underbrace{\begin{bmatrix}\delta\boldsymbol{u}_m^{n+1}\\ \delta\boldsymbol{p}_m^{n+1}\\ \delta\boldsymbol{p}_f^{n+1}\end{bmatrix}^{k}}_{\boldsymbol{\delta X}}=-\underbrace{\begin{bmatrix}\boldsymbol{R}_m^{u,n+1}\\ \boldsymbol{R}_m^{p,n+1}\\ \boldsymbol{R}_f^{p,n+1}\end{bmatrix}^{k}}_{\boldsymbol{R}} \tag{22}$$

where $\boldsymbol{J}$ is the Jacobian matrix; $\delta\boldsymbol{X}$ is the change of the primary variable vector that may be updated as

$\boldsymbol{X}^{n+1} = \boldsymbol{X}^{n} + \delta\boldsymbol{X}^{n+1,k}$ if convergence is reached; $\boldsymbol{R}$ is the residual vector; Δt is the time step size; the superscripts $\boldsymbol{u}$, p, n, and k represent displacement, pressure, time step, and Newton iteration step, respectively; the subscripts i/j and a/b denote the element and node, respectively; the subscripts m and f represent the matrix and the fracture, respectively; the symbol $()'$ represents the matrix transpose; the matrices residing in the diagonal position represent the isolated effects of each physical process (i.e., mechanical deformation and fluid flow in the matrix and the fractures) in the multi-physics system, in which $\boldsymbol{K}$ is the stiffness matrix; $\boldsymbol{E}$ and $\boldsymbol{G}$ are the compressibility matrix associated with the pressure in the matrix/fracture, respectively; and $\boldsymbol{P}$ and $\boldsymbol{U}$ are the transmissibility matrix with respect to fluid flow through the matrix/fractures, respectively. These matrices take the following expressions:

$$\boldsymbol{K}_{\boldsymbol{ab}} = \int_{\Omega_i} \left(\boldsymbol{B}_a^{\boldsymbol{u}_m}\right)^T \boldsymbol{D}\left(\boldsymbol{B}_b^{\boldsymbol{u}_m}\right) d\Omega \tag{23}$$

$$\boldsymbol{E}_{ij}^{p_m p_m} = \int_{\Omega_i} \varphi_i^{p_m} \left(\frac{\rho_f}{M}\right) \varphi_j^{p_m} d\Omega \tag{24}$$

$$\boldsymbol{G}_{ij}^{p_f p_f} = \int_{\Omega_i} \varphi_i^{p_f} \left(\frac{\rho_f}{K_n} + \frac{\rho_f w_f}{K_f}\right) \varphi_j^{p_f} d\Omega \tag{25}$$

where $\boldsymbol{D}$ is the elasticity matrix, the inverse of the compliance matrix; and $\boldsymbol{B}$ is the linearized strain operator. We adopt the embedded discrete fracture model (EDFM) to compute the inter-element flux for both fluid flow through the matrix and the fractures, including the conventional flux term $\boldsymbol{\nabla} \cdot \boldsymbol{F}$ and the leak-off term Q_L. For the sake of brevity, here we omit the derivations related to EDFM, details of which are provided in [*Li and Lee*, 2008; *Li et al.*, 2015; *Xu et al.*, 2017; *Yao et al.*, 2018]. In this technique, element pairs consist of physically neighboring connections (i.e., matrix-matrix connection (type I)) and non-neighboring connections (NNCs) (i.e., matrix-fracture connection (type II), the fracture-fracture connection of two intersecting fracture segments (type III)), and the fracture-fracture connection belonging to a single fracture (type IV), as depicted in Figure 2. The leak-off term is related to the type II connection. The inter-element flux of the fluid flow for the matrix, including the convection and leak-off terms, can be written as [*Li et al.*, 2016]:

$$\int_{\Omega} \varphi_i (\nabla \cdot \boldsymbol{F})\, d\Omega - \oiint_{\Gamma} \varphi_i \left(\rho_f \frac{k_m}{\mu} \frac{\partial (p_f - p_m)}{\partial \boldsymbol{n}_s}\right) ds = -\frac{\rho_f}{\mu} \sum_{j=1}^{nfc} \sum_{m} T_{ij,m}\, \Phi_m^{n+1} \tag{26}$$

where nfc is the total number of contact surfaces between the target element and its connected elements; $T_{ij,m}$ is the transmissibility coefficients for fluid flow; subscripts i and j denote the two main cells sharing the same flux interface; m denotes one of the contributed grid blocks associated with the face flux stencil; and $\boldsymbol{\Phi} = \boldsymbol{\nabla} p - \rho_f \boldsymbol{g}$ is the potential. The same formulation can describe fluid flow in the fractures with minor modifications. The transmissibility coefficients T_{ij} for fluid flow with respect to four types of connections, as plotted in Figure 2, have the following expressions [*Li et al.*, 2020]:

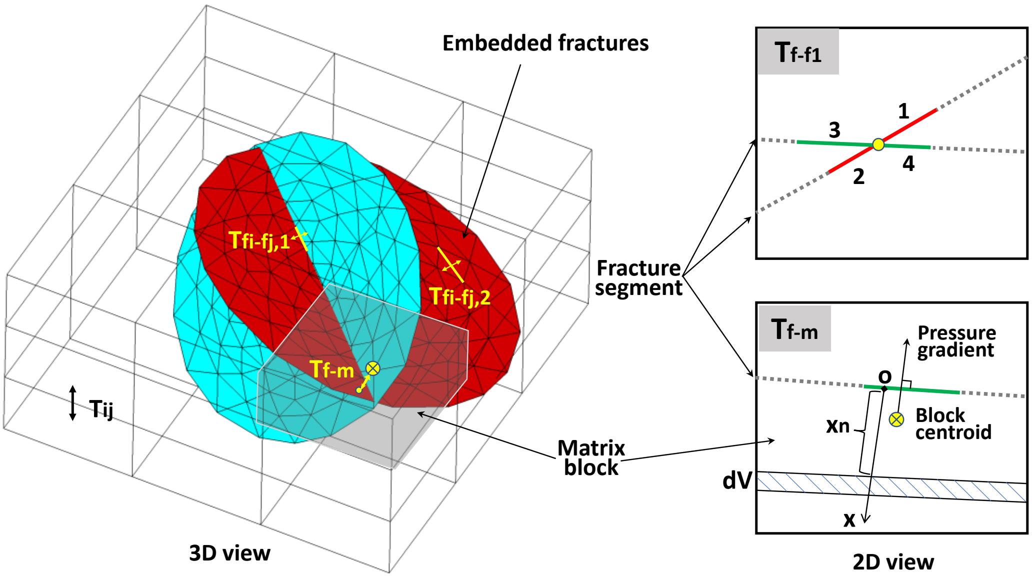

Figure 2. Schematic of the extended EDFM with four types of connections in 2-D and 3-D views (after *Li et al.* [2020]).

• Matrix-matrix connection T_{ij} (type I)

$$T_{ij} = \frac{T_1 T_2}{T_2 + T_2};\ T_i = \left(\frac{\boldsymbol{k}_m \cdot \boldsymbol{A} \cdot \boldsymbol{n}}{\boldsymbol{d} \cdot \boldsymbol{n}}\right)_i, (i = 1, 2) \tag{27}$$

• Fracture-matrix connection T_{f-m} (type II)

$$T_{f-m} = \frac{2\boldsymbol{k}_m \cdot \boldsymbol{A} \cdot \boldsymbol{n}}{\langle d \rangle};\ \langle d \rangle = V^{-1} \int_V x_n dV \tag{28}$$

• Fracture-fracture connection of two intersecting fractures T_{f-f1} (type III)

$$T_{f_i - f_j, 1} = \frac{T_1 T_2}{T_1 + T_2};\ T_i = \frac{k_{fi} A_i}{d_i}, (i = 1, 2) \tag{29}$$

• Fracture-fracture connection of an individual fracture T_{f-f2} (type IV)

$$T_{f_i - f_j, 2} = \frac{T_1 T_2}{T_1 + T_2};\ T_i = \frac{k_{fi} w_{fi} L_i}{d_{fi}}, (i = 1, 2) \tag{30}$$

$$d_{f1} = \frac{\int_{S_1} x_n dS_1 + \int_{S_2} x_n dS_2}{S_1 + S_2};\ d_{f2} = \frac{\int_{S_3} x_n dS_3 + \int_{S_4} x_n dS_4}{S_3 + S_4} \tag{31}$$

where $\boldsymbol{n}$ is the normal vector of the contact surface; $\boldsymbol{A}$ is the contact area vector; $\boldsymbol{d}$ is the distance vector pointing from the matrix grid center to the contact face center; $\langle d \rangle$ is the average normal distance from the matrix to the fracture segment (see Figure 2), with the assumption that the pressure varies linearly in the normal direction to each fracture; V is the volume of the matrix cell; dV is the volume infinitesimal of the matrix; x_n is the distance from volume infinitesimal to the fracture plane (see Figure 2); L is the length of the intersecting line of two fracture segments; k_f and w_f are the permeability and aperture of the fracture segment, respectively; d_f is the weighted average normal distance from the centroid of the fracture segment to the intersection line; A is the shared interface of these two segments; and d_1 and d_2 are the distances from the centroids of segments 1 and 2 to the shared face, respectively. Original EDFM requires high-resolution background structure grids to match the geometry of nonplanar fractures, which tends to be computationally expensive [*Zidane and Firoozabadi*, 2020]. To make the EDFM applicable for nonplanar and even twisted fractures with relatively coarse matrix grids, we have extended the algorithm in two aspects. First, the fracture segment is allowed to be much smaller than the host grid to make a twisted fracture viable within a single background grid. Second, we use triangular grids to construct a real fracture geometry such that the nonplanar 3-D fracture can be readily described and modeled. The transmissibility matrix may be expressed as follows:

$$\boldsymbol{P}_{ij}^{p_m p_m} = \frac{\partial}{\partial p_m}\left(-\frac{\rho_f}{\mu}\sum_{j=1}^{nfc}\sum_{m} T_{ij,m}\,\Phi_m^{n+1}\right) \tag{32}$$

$$\boldsymbol{U}_{ij}^{p_f p_f} = \frac{\partial}{\partial p_f}\left(-\frac{w_f\rho_f}{\mu}\sum_{j=1}^{nfc}\sum_{m} T_{ij,m}\,\Phi_m^{n+1}\right) \tag{33}$$

The non-diagonal matrix blocks are the so-called coupling matrix, which describe how one physical process affects the other one. As mentioned above, we temporarily decouple the mechanical effects of the fracture from the system. Therefore, the zero coupling matrix can be observed in the Jacobian matrix of Eq. (22). The non-zero coupling matrix may be written as:

$$\boldsymbol{L}_{ia}^{p_m \boldsymbol{u}_m} = \int_{\Omega_i} \varphi_i^{p_m} b(\nabla\psi_a^{\boldsymbol{u}_m})\mathrm{d}\Omega \tag{34}$$

$$\boldsymbol{S}_{ij}^{p_m p_f} = -\int_{\Omega_i} \varphi_i^{p_m}\left(\frac{\rho_f T_{m_i-f_j}}{\mu}\right)\varphi_j^{p_f}\mathrm{d}\Omega \tag{35}$$

3.2 Discretization of Nonplanar 3-D Fractures Allowing for Fracture Deformation

In Section 3.1, the FVFEM is employed to compute the pore pressure in the matrix, the fluid pressure in the fractures, and the stress state of the matrix. The aperture change is then estimated by BEM with known stress boundary conditions rendered by FVFEM. A fracture is discretized into a set of triangular grids. With prescribed boundary stresses applied on fracture surfaces, the normal and shear displacements of these grids may be evaluated by solving the following equations in the local coordinate system:

$$\begin{bmatrix} \vdots \\ \sigma_{n,locf}^{i} \\ \tau_{s,locf}^{i} \\ \tau_{t,locf}^{i} \\ \vdots \end{bmatrix} = \begin{bmatrix} & \vdots & \\ \sum_{j=1}^{N} \left\{ \begin{bmatrix} C_{nn}^{ij} & C_{ns}^{ij} & C_{nt}^{ij} \\ C_{sn}^{ij} & C_{ss}^{ij} & C_{st}^{ij} \\ C_{tn}^{ij} & C_{ts}^{ij} & C_{tt}^{ij} \end{bmatrix} \begin{bmatrix} D_n^j \\ D_s^j \\ D_t^j \end{bmatrix} \right\} \\ & \vdots & \end{bmatrix}, (i, j = 1, \cdots, N) \tag{36}$$

where C is the influence coefficient; D is the displacement discontinuity; σ and τ are the normal and shear stresses, respectively; the superscripts i and j denote the numbering of the fracture segment grid; the subscripts n, s, and t denote the directions of normal opening, strike-slip shear, and dip-slip shear, respectively; the subscript symbol '$locf$' denotes a variable for the fracture segment in the local coordinate system; and N is the total number of triangular fracture elements. Therefore, C_{nn}^{ij} represents the influence coefficient that links the normal displacement at element j to the normal displacement at element i (cf. Figure 3a). The expressions for influence coefficients can be found in *Fan et al.* [2020], in which a mixed analytical and numerical approach is employed to solve the kernel functions for estimating the influence coefficient. It is found that this approach is 32% faster than that of the pure numerical method. The displacements for each element are defined in the element-local coordinate. As is illustrated in Figure 3b, one of the edges of the triangular element *j* is chosen as the x-axis (i.e., with the same direction of the $\boldsymbol{x}_1$ vector); and thus the z-axis (the $\boldsymbol{x}_3$ vector) can be defined by the cross product of the vector $\boldsymbol{x}_1$ and the edge vector $\boldsymbol{x}_m$, and the y-axis (the $\boldsymbol{x}_2$ vector) is represented by the cross product of the vector $\boldsymbol{x}_3$ and the vector $\boldsymbol{x}_1$. We then define the displacement discontinuities of the j-th fracture element in the local coordinate system as follows [*Kuriyama and Mizuta*, 1993]:

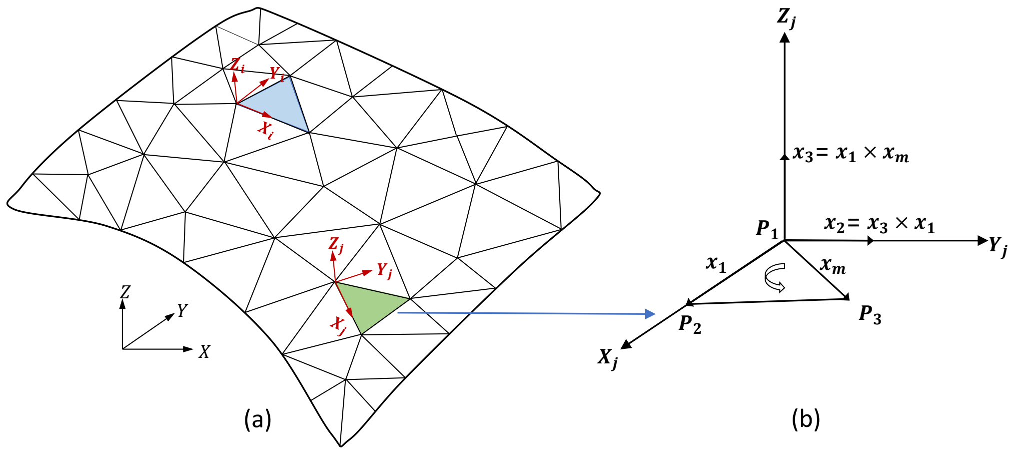

Figure 3. Illustration of local and global coordinates of 3-D BEM based on triangular elements: (a) a pair of triangle elements in the global coordinate system selected to calculate influence coefficients; and (b) setup of the local coordinate system for element *j*.

$$\begin{bmatrix} D_n^j \\ D_s^j \\ D_t^j \end{bmatrix} = \begin{bmatrix} (u_z)_{z=0^-} - (u_z)_{z=0^+} \\ (u_y)_{y=0^-} - (u_y)_{y=0^+} \\ (u_x)_{x=0^-} - (u_x)_{x=0^+} \end{bmatrix} \tag{37}$$

where u is the displacement; and the superscripts '$-$' and '$+$' denote values on the negative and positive side of the fracture, respectively. Note that the normal displacement discontinuity is equivalent to the fracture aperture, i.e., $w_f = D_n = (u_z)_{z=0^-} - (u_z)_{z=0^+}$. Based on the simulation results from (22), the boundary stress conditions associated with the i-th fracture element are expressed as:

$$\begin{bmatrix} \sigma_{n,locf}^i \\ \tau_{s,locf}^i \\ \tau_{t,locf}^i \end{bmatrix} = \begin{bmatrix} (p_f^i - p_m^l) + \sigma_{n,locm}^l \\ \tau_{s,locm}^l \\ \tau_{t,locm}^l \end{bmatrix} \tag{38}$$

where p_f^i is the fluid pressure in the i-th fracture element; p_m^l is the pore pressure in the l-th matrix element, into which the i-th fracture element is embedded; and the subscript '$locm$' denotes a variable with respect to the matrix in the local coordinate system. The stresses, on the fracture surface, can be calculated by transforming the stress tensor of the matrix block from the global coordinate system to the local one:

$$\begin{bmatrix} \sigma_{n,locm}^l & \tau_{s,locm}^l & \tau_{t,locm}^l \end{bmatrix}' = \left(\boldsymbol{M}_i[\boldsymbol{\sigma}'_{ij,m}]\boldsymbol{M}'_i\right) \cdot \boldsymbol{n}_s \tag{39}$$

where $\boldsymbol{\sigma}'_{ij,m}$ is the effective stress tensor of the matrix block, bounding the fracture element with the normal vector $\boldsymbol{n}_s$; and $\boldsymbol{M}_i$ is a transformation matrix that converts the stress from the global coordinate to the local coordinate of the i-th fracture element.

4. Nonplanar 3-D Fracture Growth and Iteratively Coupled Solution

4.1 Stress Intensity Factors and Fracture Growth

Fracture growth in rock mass relies on the singular stress field in the vicinity of the fracture tip, which can be characterized by stress intensity factors (SIFs). Based on the theory of linear elastic fracture mechanics (LEFM), SIFs are estimated by fracture tip displacements or fracture tip stresses with three fundamental fracturing modes, i.e., tensile, in-plane shear, and anti-plane shear. Since the fracture tip displacements are determined by Eq. (36) using BEM at the end of each time step, we employ the displacement-based approach to extract SIFs as follows [*Olson and Taleghani*, 2009]:

$$K_{\mathrm{I}} = \frac{\xi D_n E\sqrt{\pi}}{4(1-\nu^2)\sqrt{2r}};\ K_{\mathrm{II}} = \frac{\xi D_s E\sqrt{\pi}}{4(1-\nu^2)\sqrt{2r}};\ K_{\mathrm{III}} = \frac{\xi D_t E\sqrt{\pi}}{4(1+\nu)\sqrt{2r}} \tag{40}$$

where E is Young's modulus; ν is Poisson's ratio; r is the distance from the centroid of the triangular element to the fracture propagation front; and ξ=0.806 is an empirical constant, suggested by *Olson and Taleghani* [2009]. In this work, we use the maximum principal stress criterion, proposed by *Schöllmann et al.* [2002], to predict the nonplanar 3-D fracture propagation. This criterion shows that the fracture growth occurs when stress intensity factor K_{eq} reaches a critical value, i.e., the fracture toughness K_{IC}:

$$K_{IC} \geq K_{eq} = \frac{1}{2}\cos\left(\frac{\gamma_0}{2}\right)\left\{K_{\mathrm{I}}\cos^2\left(\frac{\gamma_0}{2}\right) - \frac{3}{2}K_{\mathrm{II}}\sin(\gamma_0) + \sqrt{\left[K_{\mathrm{I}}\cos^2\left(\frac{\gamma_0}{2}\right) - \frac{3}{2}K_{\mathrm{II}}\sin(\gamma_0)\right]^2 + 4K_{\mathrm{III}}^2}\right\} \tag{41}$$

where γ_0 is the fracture deflection angle under multiaxial loading. According to *Schöllmann et al.* [2002], the fracture propagation direction is perpendicular to the maximum principal stress (tensile stress is positive) σ_1', given by [*Schöllmann et al.*, 2002]:

$$\sigma_1' = \frac{\sigma_\gamma + \sigma_z}{2} + \frac{1}{2}\sqrt{\left(\sigma_\gamma - \sigma_z\right)^2 + 4\tau_{\gamma z}^2} \tag{42}$$

The deflection angle yields:

$$\frac{\partial \sigma_1'}{\partial \gamma}\Big|_{\gamma=\gamma_0} = 0; \ \frac{\partial^2 \sigma_1'}{\partial \gamma^2}\Big|_{\gamma=\gamma_0} < 0 \tag{43}$$

Combining the tip-induced stresses and far-field stresses, the near-tip stress field is expressed as:

$$\begin{bmatrix} \sigma_\gamma \\ \sigma_z \\ \tau_{\gamma z} \end{bmatrix} = \begin{bmatrix} \sigma_\gamma^r \\ \sigma_z^r \\ \tau_{\gamma z}^r \end{bmatrix} + \begin{bmatrix} \sigma_\gamma^t \\ \sigma_z^t \\ \tau_{\gamma z}^t \end{bmatrix} \tag{44}$$

where σ_γ, σ_z, and $\tau_{\gamma z}$ are the local stress components in a cylindrical coordinate system at the fracture tip; and the superscripts *r* and *t* denote the remote and tip stress field, respectively. The remote stress can be extracted from the host matrix block of the fracture front element; and the expressions for the tip-induced stresses are given in *Schöllmann et al.* [2002]. After solving the deflection angle γ_0 based on Eqs. (42) through (44), the equivalent SIF K_{eq} will be available for determining the magnitude of fracture advancement [*Cherny et al.*, 2016]:

$$\Delta L = L_{max}\left(\frac{K_{eq}}{K_{IC}}\right)^m \tag{45}$$

where L_{max} is the fracture front advancement magnitude when the critical SIF K_{IC} occurs; and m is the material constant (m=1.0 used this work).

4.2 Solution Strategy

An iteratively coupled method is proposed to solve the above equation system associated with nonplanar

3-D fracture propagation in poroelastic media, as shown in Figure 4. In this approach, we first solve the pressure in the matrix and the fractures (i.e., p_m and p_f), as well as the stress distribution (i.e., σ'_m) in the matrix, using FVFEM [*Li et al.*, 2016]. The calculated pressure and the stress provide the boundary conditions of the BEM, with which we compute the fracture aperture, the fracture stiffness, and fracture-induced stresses. Therefore, this solution scheme constitutes a two-way coupling approach (cf. Figure 4). The former renders the mechanical boundary conditions for the latter, and the latter, in turn, provides the fracture aperture and fracture stiffness that are significant parameters for the former to close the mass balance equation associated with the fracture element.

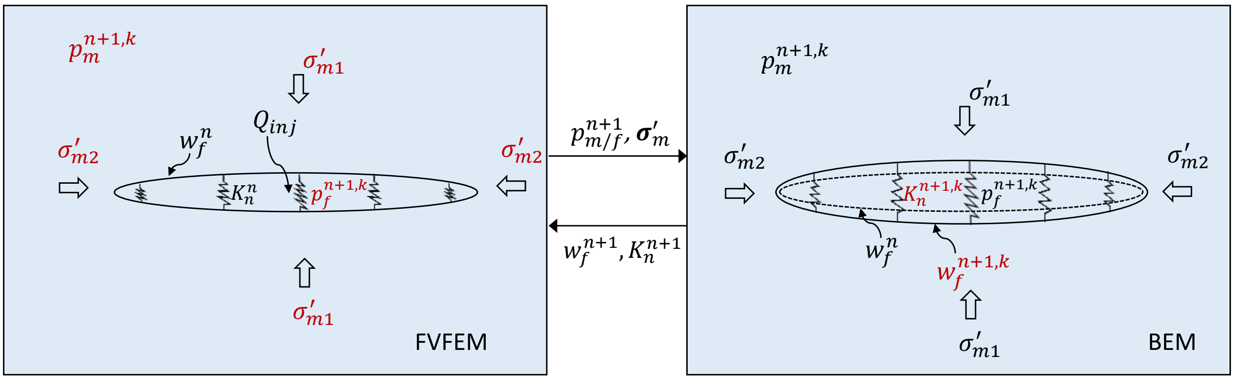

Figure 4. Schematic of the iteratively coupled approach for the fracture propagation problem.

Figure 5 summarizes the implementation in C++ of the solution of the nonplanar 3-D fracture propagation problem, considering fluid flow in the matrix and the fracture, and the fluid exchange between them. Initialization of the model comprises two steps: the first step utilizes the prescribed hydraulic/mechanical boundary conditions and the initial pressure condition to initialize the poroelastic model; in the second step, the fracture aperture and the fracture permeability could be initialized, using the calculated pressure in the matrix/fracture and the stress in the matrix of the first step. After initialization, we proceed to the iteratively coupled algorithm (ref. Figure 4), in which coupling parameters between the FVFEM and BEM modules are mapped to each other at the Newton-iteration level.

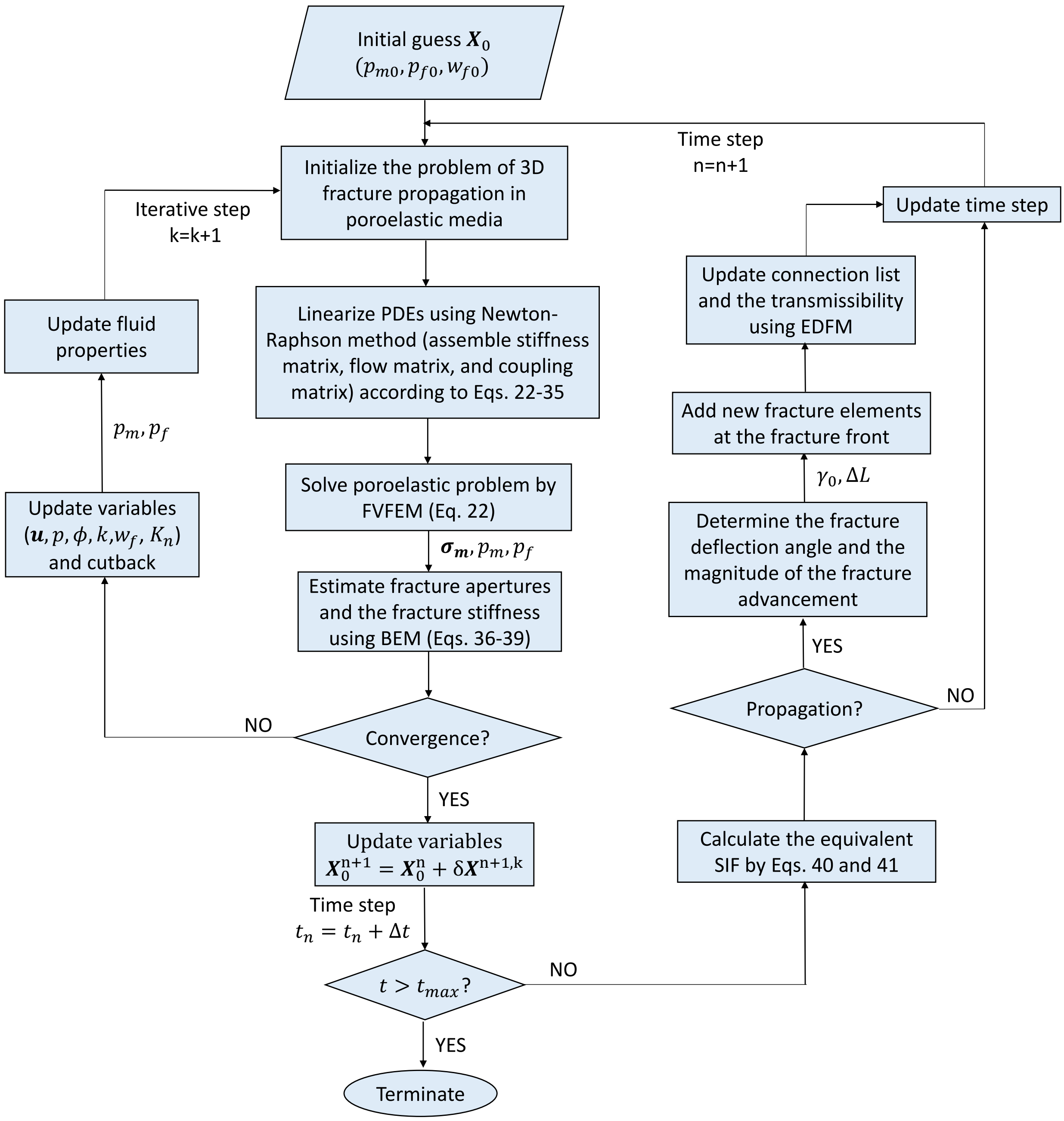

Figure 5. Flow chart for solving the propagation of nonplanar 3-D fractures in poroelastic media.

As mentioned in Section 2.3, the aperture change $\partial w_f / \partial t$ provides an essential step in coupling. For closed fractures, we adopt Eq. (16) to explicitly update the fracture stiffness and fracture aperture. For open fractures, the BEM is utilized to solve them via Eqs. (36) through (38). Based on the definition of the derivative, the fracture stiffness is expressed as follows:

$$K_n = \lim_{\delta p_f \to 0} \left(\frac{\delta p_f}{\delta w_f} \right) \tag{46}$$

After solving the FVFEM module to obtain the fluid pressure p_f and the stress $\boldsymbol{\sigma}'_m$ during an iteration step, the BEM module is then employed to compute the fracture aperture w_f. A small fluid pressure perturbation δp_f (e.g., 100 Pa used in this model) is introduced to the system to yield another fracture aperture w_f'. The fracture stiffness for the current iteration step is then obtained:

$$K_n = \frac{\delta p_f}{w_f' - w_f} \tag{47}$$

The known fracture aperture and fracture stiffness allow us to proceed to the next iteration step until the convergence criterion is satisfied:

$$\frac{\|\boldsymbol{X}^{n+1,k} - \boldsymbol{X}^n\|}{\|\boldsymbol{X}^{n+1,k}\|} < \varepsilon_{HM};\ \frac{\|\boldsymbol{w}_f^{n+1,k} - \boldsymbol{w}_f^n\|}{\|\boldsymbol{w}_f^{n+1,k}\|} < \varepsilon_{w_f} \tag{48}$$

where $\varepsilon_{HM} = 0.01$ and $\varepsilon_{w_f} = 0.01$ are the specified tolerances for the FVFEM module and the BEM module, respectively; and the symbol '$\|\cdot\|$' denotes the operator for root mean square. If the convergence conditions are satisfied, the variables should be updated, $\boldsymbol{X}_0^{\mathrm{n}+1} = \boldsymbol{X}_0^{\mathrm{n}} + \delta \boldsymbol{X}^{\mathrm{n}+1,\,k}$, as the initial guess of the next time step and the simulation time should also be updated. The updated fracture apertures will assist to estimate three fundamental SIFs (Eq. (40)) and the equivalent SIF (Eq. (41)) of the fracture front element. If the maximum equivalent SIF falls within a specified range [*Gupta and Duarte*, 2018]:

$$K_{eq}^{max} = max\left\{K_{eq}^1, \cdots, K_{eq}^i, \cdots, K_{eq}^N\right\} \in [(1-\theta)K_{IC}, (1+\theta)K_{IC}] \tag{49}$$

where θ is a model constant ($\theta = 0.05$ used in this work). The fracture is allowed to propagate with the magnitude ΔL^i which is estimated by Eq. (45) and the deflection angle γ_0^i is given by finding the maximum principal stress based on Eqs. (42) through (44). A ring-shaped fracture front, composed of a series of triangular elements, is added to the fracture. These newly generated elements are marked as fracture tips, which are used for estimating the maximum equivalent SIF of the subsequent propagation step. Moreover, the EDFM algorithm [*Li et al.*, 2015; *Yao et al.*, 2018] is employed to search for additional connections related to these new fracture elements. Accordingly, the connection list and the transmissibilities that are used for constructing the Jacobian matrix should be updated for the next time step. On the other hand, if the K_{eq}^{max} does not fall into the specified range, we then need to adjust the time step for better convergent performance.

5. Validation of the Hybrid Model

5.1 Horizontal Penny-Shaped Fracture Growth: Verification Example 1

Savitski and Detournay [2002] derived an asymptotic expression for penny-shaped fracture propagation in impermeable media with the assumptions of an incompressible fluid, linear elastic rock, and no fluid lag at the fracture tip. In this approach, a dimensionless viscosity is defined to distinguish the viscosity-dominated from the toughness-dominated propagation regimes [*Savitski and Detournay*, 2002]:

$$M_{\mu} = \mu' \left(\frac{Q_0^3 E'^{13}}{K'^{13} t^2} \right)^{1/5} \tag{50}$$

where Q_0 is the injection rate; $E' = E/(1-\nu^2)$ is the plane-strain elastic modulus; t is the injection time; and two material parameters $\mu' = 12\mu$ and $K' = 4\sqrt{2/\pi}\, K_{IC}$. For $M_{\mu} \gg 1$, most of the energy, provided by the hydraulic fluid, is dissipated in viscous fluid flow (i.e., viscosity-dominated); $M_{\mu} \ll 1$ is an indication that the creation of a new fracture surface requires most of the energy (i.e., toughness-dominated). In this example validation, we inject a fluid of viscosity μ=1.0 cP at a constant rate Q_0=0.01 m^3/s at the center of a penny-shaped fracture with an initial radius R_0=1.0 m. The rock toughness, Young's modulus, and Poisson's ratio are K_{IC}=1.0 MPa/$\sqrt{m}$, E=38.8 GPa, and ν=0.15, respectively.

Eq. (50) shows that M_{μ} is time-dependent and decreases with time. At t=1.0 s, the dimensionless viscosity M_{μ}= 0.0825 $\ll 1$, which demonstrates that when $t \geq$1.0 s the asymptotic solution for the toughness-dominated regime could serve as a good benchmark. The allowed growth advancement for each propagation step is L_{max}=1.0 m. The total injection time is 124 s, during which the radial fracture experiences 43 propagation steps and its radius is extended to *R*=41.8 m. The created fracture has a maximum aperture w_f=0.84 mm at the center location, as shown in Figure 6a. Panels 6b through 6d in Figure 6 show that the numerical results are very close to the analytical solutions for the fracture radius, the fracture aperture at the injection point, and the net pressure (fluid pressure minus the remote stress). The predictions by the proposed model in planar fracture growth are in agreement with the analytical solutions. To examine predictions of nonplanar 3-D fracture propagation, we present an inclined radial fracture growth problem as follows.

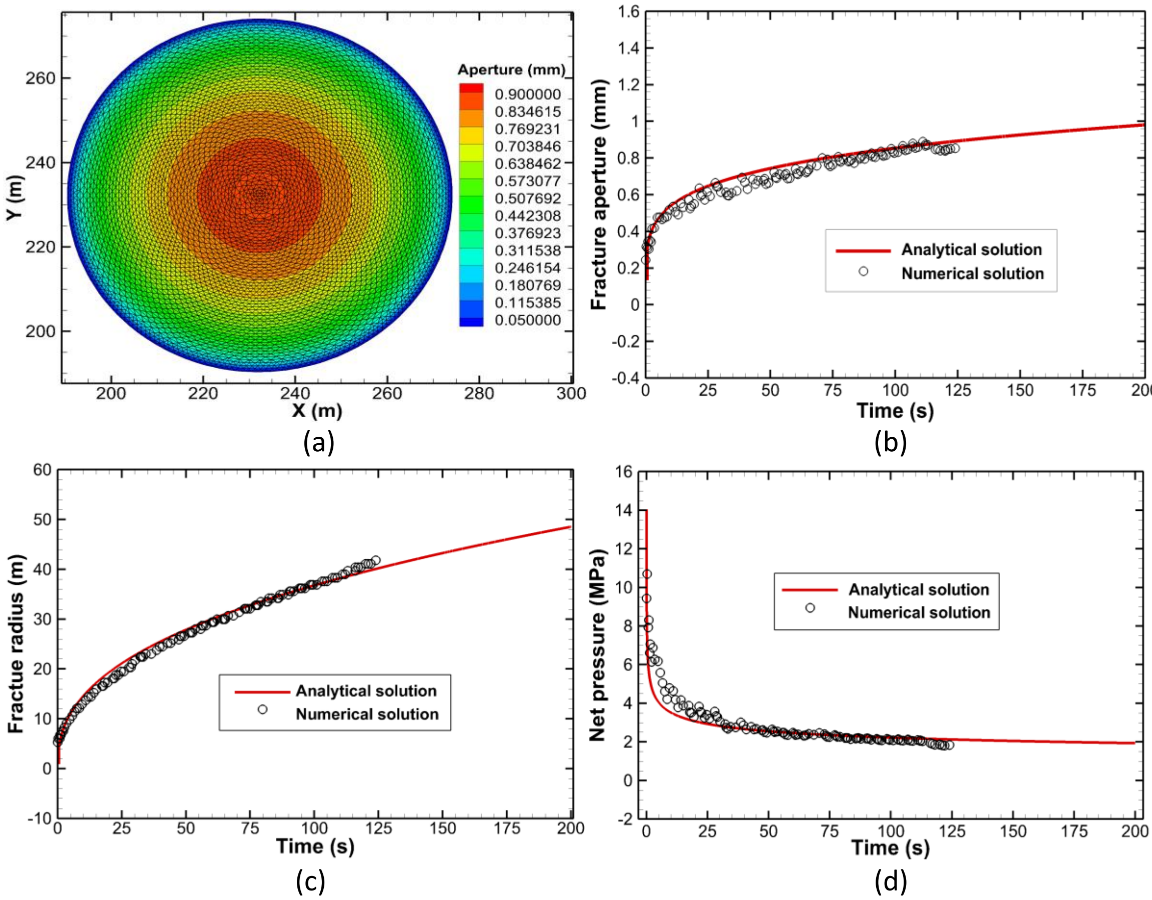

Figure 6. Numerical results and analytical solution for the penny-shaped fracture growth problem: (a) numerical result of the fracture aperture distribution after 43 propagation steps (at 124 s); (b) history plots of fracture aperture at the injection point; (c) history plot of the fracture radius; and (d) net pressure profile at the injection point. Verification Example 1.

5.2 Inclined Penny-Shaped Fracture Growth: Verification Example 2

For nonplanar 3-D fracture propagation, there are no available analytical solutions for benchmarking. The exact solution of SIFs for the onset of an inclined fracture growth under uniaxial tensile stress is presented in [*Kassir and Sih*, 1975]:

$$
\begin{aligned}
K_I &= 2\sigma_z \cos^2\alpha \sqrt{R/\pi} \\
K_{II} &= \frac{2}{2-\nu}\sigma_z \sin2\alpha \cos\omega \sqrt{R/\pi} \\
K_{III} &= \frac{2(1-\nu)}{2-\nu}\sigma_z \sin2\alpha \sin\omega \sqrt{R/\pi}
\end{aligned}
\tag{51}
$$

where α is the fracture dip angle; ω is an angular coordinate on the fracture plane as shown in Figure 7a; and σ_z is the remote stress along the z-axis. This solution has been widely used in the literature [*Cherny et al.*, 2016; *Krysl and Belytschko*, 1999; *Shi and Shen*, 2018; *Tang et al.*, 2019; *Thomas et al.*, 2017] to validate nonplanar fracture propagation. In our validation, we apply a remote tensile stress σ_z=2.5 MPa on the upper and lower boundaries of the target domain, as depicted in Figure 7a. The rock toughness and Poisson's ratio are K_{IC}=1.0 MPa/$\sqrt{m}$ and ν=0.25, respectively. Figure 7b shows good agreement between the numerical results and the analytical solutions for the first propagation step. We simulate the subsequent propagation steps, as shown in Figure 8, in which we observe that the inclined fracture gradually rotates into the direction perpendicular to the maximum principal stress (tensile is positive). Similar modeling results have been reported by *Krysl and Belytschko* [1999], *Gupta and Duarte* [2014], *Cherny et al.* [2016], *Shi and Shen* [2018], and *Thomas et al.* [2020a], which further confirms the reliability of the proposed model.

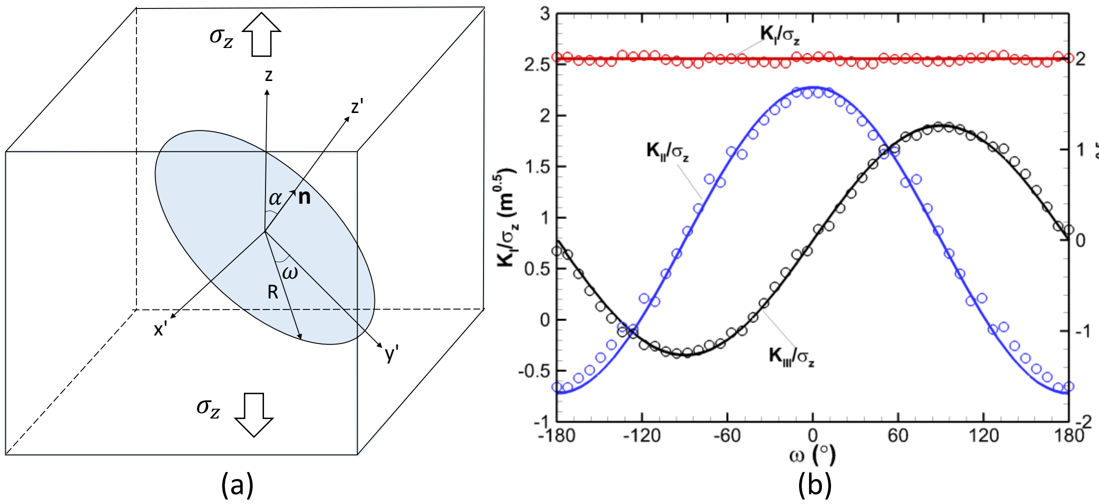

Figure 7. Inclined penny-shaped fracture growth problem: (a) schematic of an inclined penny-shaped fracture with a dip angle of α=30° and an initial radius of R=9.1 m; and (b) simulation results (circle) and the analytical solutions (solid line) of scaled stress intensity factors for three different propagation modes: Verification Example 2.

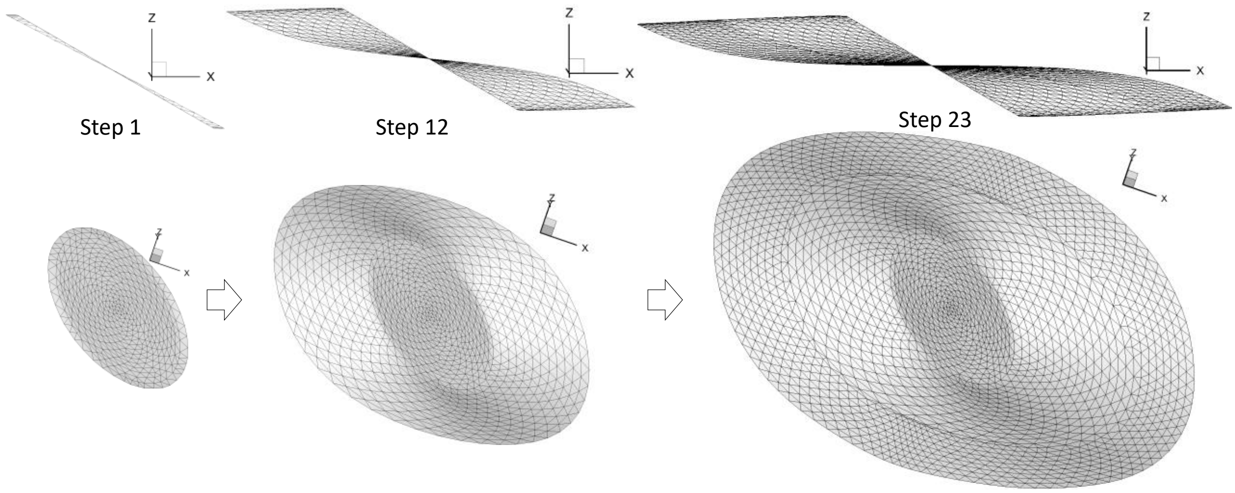

Figure 8. Simulation results of geometries of the propagating nonplanar fracture at various advancement steps in side view and 3-D view: Verification Example 2.

6. Numerical Results

6.1 Example 1: Planar Fracture's Propagation in Three Stress Layers

Fluid-driven fracture propagation in multilayer formations is of great interest in the petroleum/geothermal industry. Related scientific/engineering issues include the fracture growth rate, the fracture's footprint, and the fracture aperture distribution. For underground storage projects, e.g., carbon dioxide sequestration, a vertically propagating hydraulic fracture should be either contained in the reservoir rock or allowed to extend a limited height into the caprock, improving injectivity and guaranteeing the integrity of the caprock in the long-term, as well [*Fu et al.*, 2017]. Development of unconventional resources necessitates hydraulic fracturing treatments in the reservoirs to enhance the permeability, and thus the productivity. Fracturing engineers anticipate that the created fractures are constrained in target formations for improving the effectiveness of fracturing treatments. *Fisher and Warpinski* [2012] reported several fracture-containment mechanisms, such as material-property contrast (e.g., fracture toughness and Young's modulus), weak interface (e.g., bedding plane, faults, fractures, and veins), permeability contrast, fluid-pressure gradient, and *in-situ* stress contrast. In this example, we investigate planar fracture's propagation under vairous *in-situ* stress contrasts.

Figure 9a portrays a three-layer formation with distinct principal stresses, σ_1^h, σ_2^h, and σ_3^h, with the same Young's modulus E=20 GPa, and Poisson's ratio ν=0.25. Other relevant data are: injection rate Q_0=0.01 m^3/s; fluid viscosity μ=10 mPa·s; fracture toughness K_{Ic}=1.0 MPa$\sqrt{m}$; matrix permeability 10^{-2} mD; and maximum front advancement L_{max}=1.0 m. Three cases associated with the stress condition are designed as [*Dontsov and Peirce*, 2017]:

- Case 1: $\sigma_1^h = 7.75$ MPa, $\sigma_2^h = 7.0$ MPa, and $\sigma_3^h = 7.75$ MPa.
- Case 2: $\sigma_1^h = 7.75$ MPa, $\sigma_2^h = 7.0$ MPa, and $\sigma_3^h = 7.25$ MPa.
- Case 3: $\sigma_1^h = 7.25$ MPa, $\sigma_2^h = 7.0$ MPa, and $\sigma_3^h = 6.5$ MPa.

Panels 9b through 9d in Figure 9 show the simulation results to 560 s, corresponding to symmetric stress barriers (Case 1), asymmetric stress barriers (Case 2), and monotonous stress (Case 3), respectively. Symmetric fracture geometry is induced in Case 1, while asymmetric fracture footprints are observed in Cases 2 and 3. The fracture propagates more extensively and possesses a larger width within the layer with a lower minimum principal stress, which demonstrates that the stress affects the fracture growth rate, so as the fracture geometry. As shown in Figure 10, the ring-shaped fracture front is characterized as various magnitudes at different locations for the 28th growth step, which indicates the growth rate at the fracture tip. For example, the light blue stripe in Figure 10, related to Case 3, displays that a minimum advancement of L=0.17 m is observed in layer #1. The magnitude of the advancement gradually increases from the minimum to L=0.42 in layer #2, and then to the maximum L=1.0 m in layer #3. The reason behind these results is the stress-controlled displacement discontinuity at different locations. A higher stress would cause a larger displacement discontinuity, which results in a larger advancement at the fracture tip according to Eqs. (40) and (45).

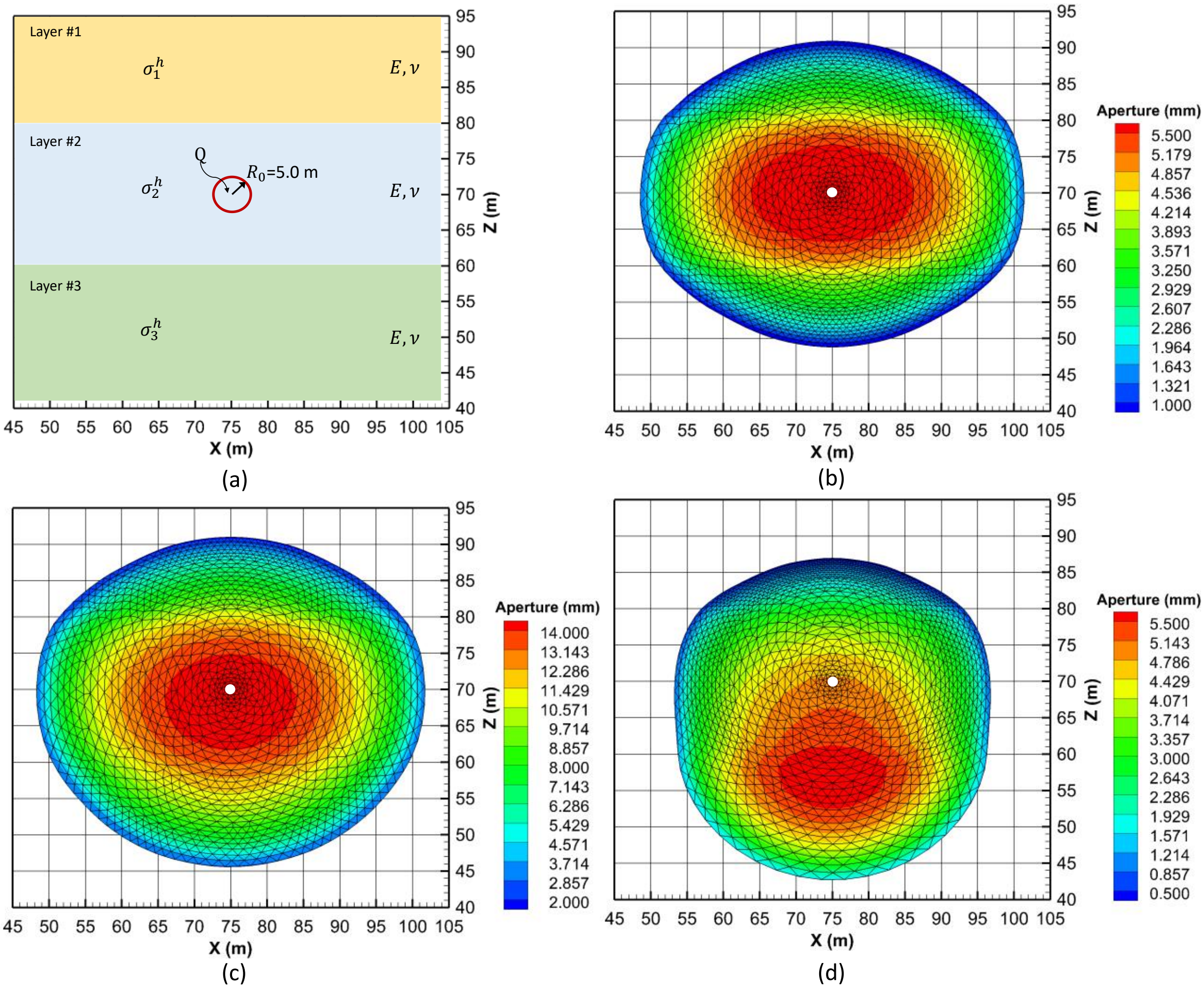

Figure 9. Planar fractures with different footprints and aperture distributions, induced by various layered stress conditions, after 28 propagation steps (at 560 s): (a) schematic of layered stress condition; (b) symmetric stress barriers; Case 1 (c) asymmetric stress barriers; Case 2, and (d) monotonous stress, Case 3. Note that the injection point is located at (x, z)~(75 m, 70 m), i.e., the center of the radial fracture (the red circle) with an initial radius of 5.0 m, and that the white dots in panels (b) through (d) denote the injection points: Example 1.

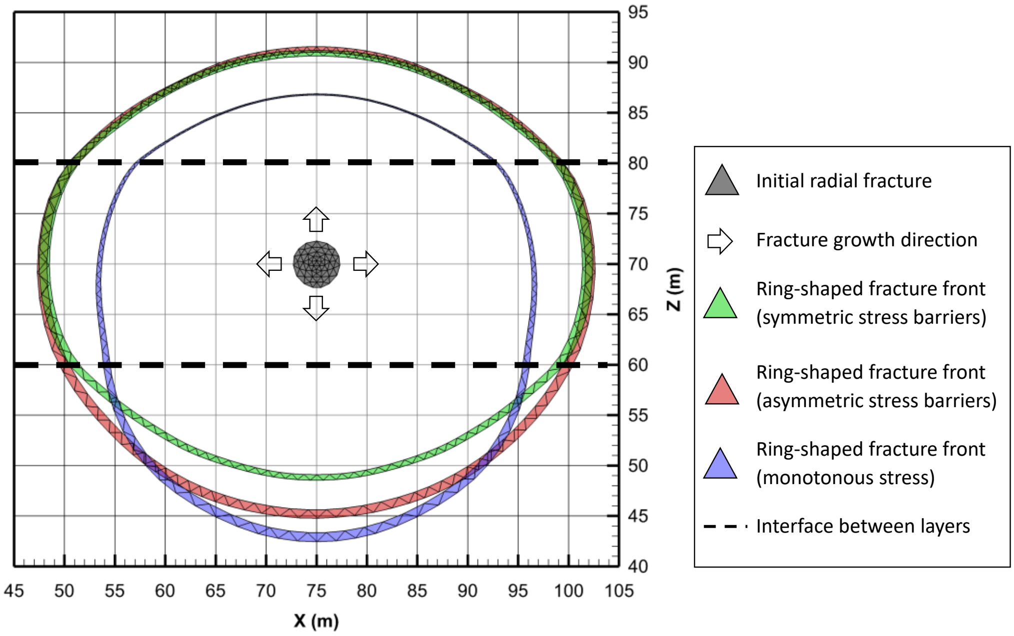

Figure 10. Ring-shaped fracture fronts after 28 propagation steps (at 560 s) for various layered stress conditions: Example 1.

6.2 Example 2: Propagation from Two-Parallel Fractures under Stress Anisotropy

In Example 2, we investigate nonplanar 3-D fracture propagation, induced by the stress shadowing effect. It is assumed that two parallel fractures with an initial radius of 5.0 m and a distance of 5.0 m, connected by a vertical well, reside in a stratum with a thickness of 30 m, as depicted in Figure 11. The stratum is located at a relatively shallow depth (i.e., 300 m) such that the vertical stress is the minimum compressive stress, which belongs to a reverse-fault environment (i.e., $S_V = 7.5$ MPa < $S_h = 8.5$ MPa $< S_H = 12.5$ MPa). The domain has a dimension of $100\ \mathrm{m} \times 100\ \mathrm{m} \times 30\ \mathrm{m}$, which is discretized into $30 \times 30 \times 10 = 9000$ identical matrix blocks. Other parameters are listed in Table 1.

Table 1

Various parameters: Example 2.

Parameters	Value	Unit
Injection rate Q	0.02	m^3/s
Matrix permeability k_m	0.1	mD
Fluid density	1000	kg/m^3
Fluid viscosity μ	1.0	mPa·s
Fluid compressibility $1/K_f$	5.0×10^{-10}	1/Pa
Biot coefficient b	0.85	-
Initial fluid pressure $p_{f/m}$	4.0	MPa
Porosity ϕ	0.25	-
Young's modulus E	20.0	GPa
Poisson's ratio ν	0.2	-
Fracture toughness K_{Ic}	1.5	$\mathrm{MPa}\sqrt{m}$
Maximum advancement L_{max}	1.0	m

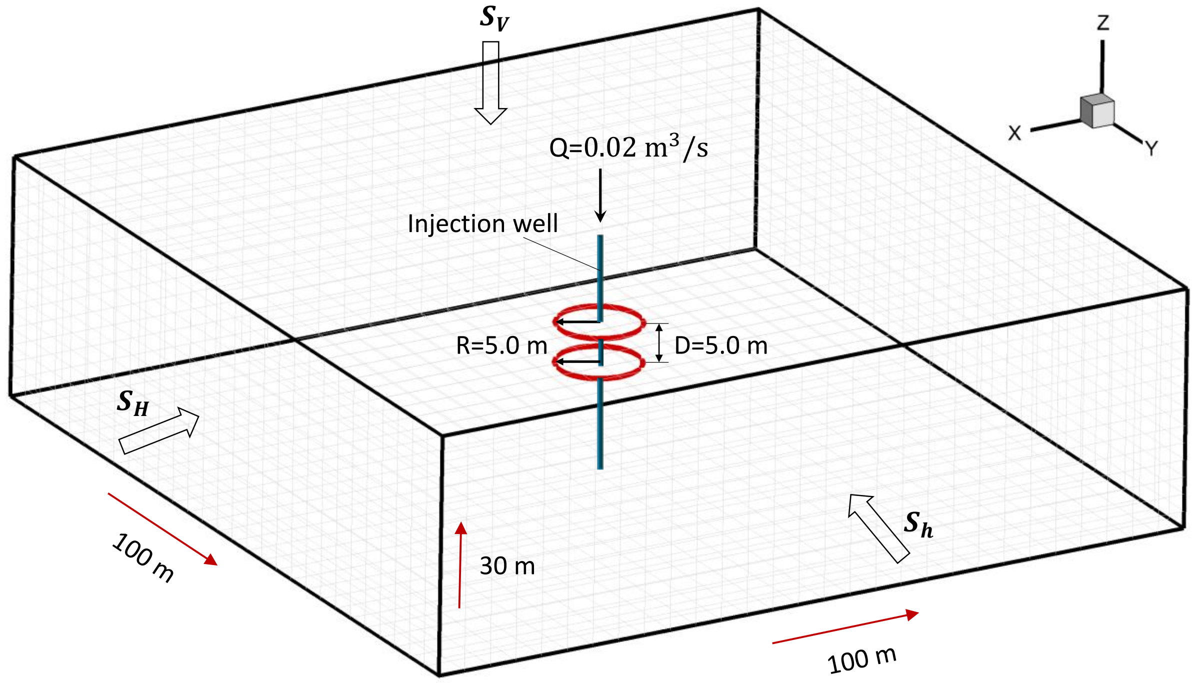

Figure 11. Illustration of the physical model for two parallel fractures (red circles) linked by a single vertical well: Example 2.

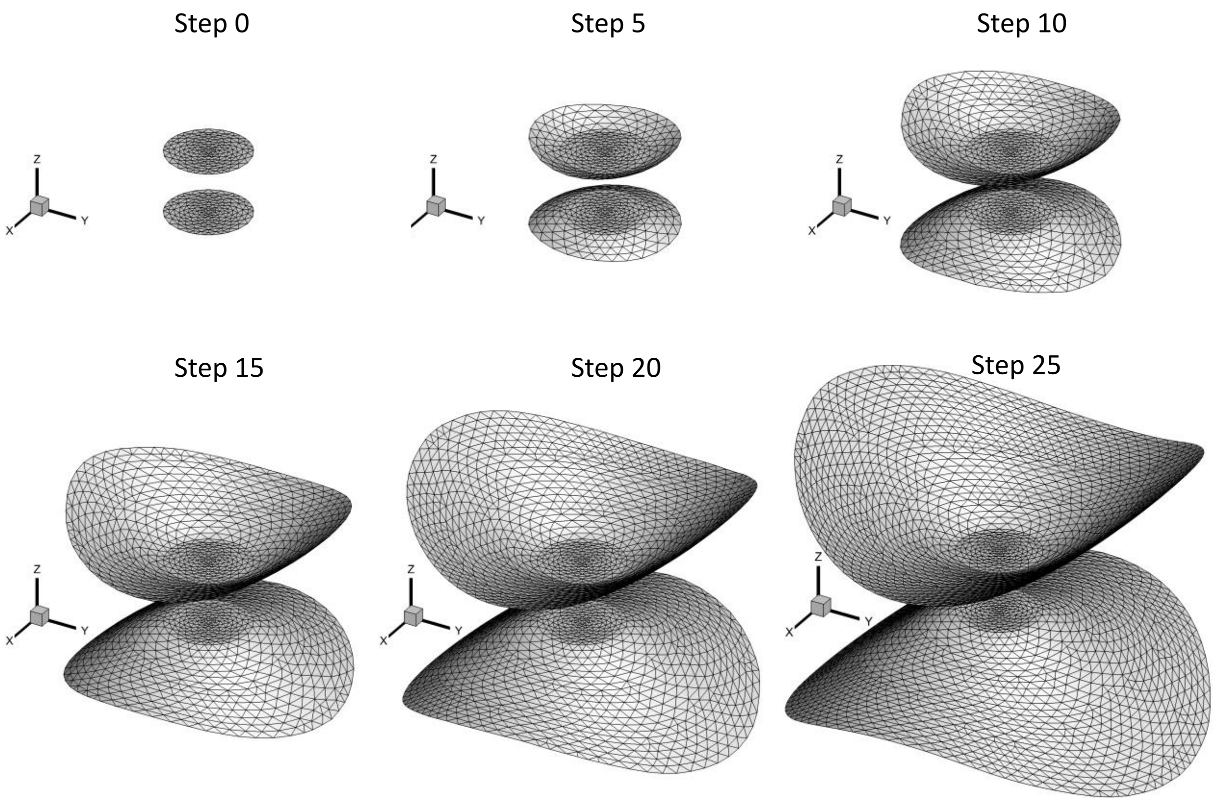

Figure 12. Geometries of the propagating nonplanar fractures at various advancement steps in side 3-D view: step 0 (0 s), step 5 (105 s), step 10 (257 s), step 15 (430), step 20 (655 s), and step 25 (930 s): Example 2.

The total simulation time is 930 s, during which the geometries of two interactional fractures at different growth steps/times are plotted in Figure 12. One can observe from these simulation results that the two fractures propagate apart from each other seeking a path with the least resistance, and that the difference of growth rate at fracture tips of different locations leads to asymmetric geometries. Figure 13 depicts the sampled points for extracting the stress distribution and the fracture-induced stress change along the *z*-axis. The stress experiences a decrease in the regions ahead of the fracture front, but a significant increase in the vicinity of the fracture along its normal direction; this is the major reason why we set densely sampled points in the vicinity of the fracture and the fracture front, as shown in panels (A) and (B) of Figure 13. This strategy has an advantage in reducing the computation time for stress extraction by BEM over evenly collecting the sampled points, especially in 3-D. Figure 14 shows the fracture aperture distribution after 25 growth steps (at 930 s). This figure conveys three points: the first is that two competing fractures simultaneously propagate with a very close growth rate at their symmetric locations; the second is that, for each of the fractures, different growth rates from the stress difference, as analyzed in Section 6., result in an asymmetric geometry (comparison of Figure 14b and Figure 14c); and the final point is that the stress interaction (cf. Figure 13) tends to change the local stress state, as well as the propagation direction, resulting in a nonplanar fracture. Figure 15 shows the effect of matrix gridding after 25 growth steps in four different gridding sets. There is no appreciable difference in the fracture geometry, fracture size, and fracture deflection. There is a slight difference in the fracture aperture distribution, i.e., at higher matrix grid resolution the fracture aperture is smaller. A coarser matrix grid in the vicinity of the fracture would underestimate the magnitude of the leakoff, which causes a higher net pressure and a larger fracture aperture as well.

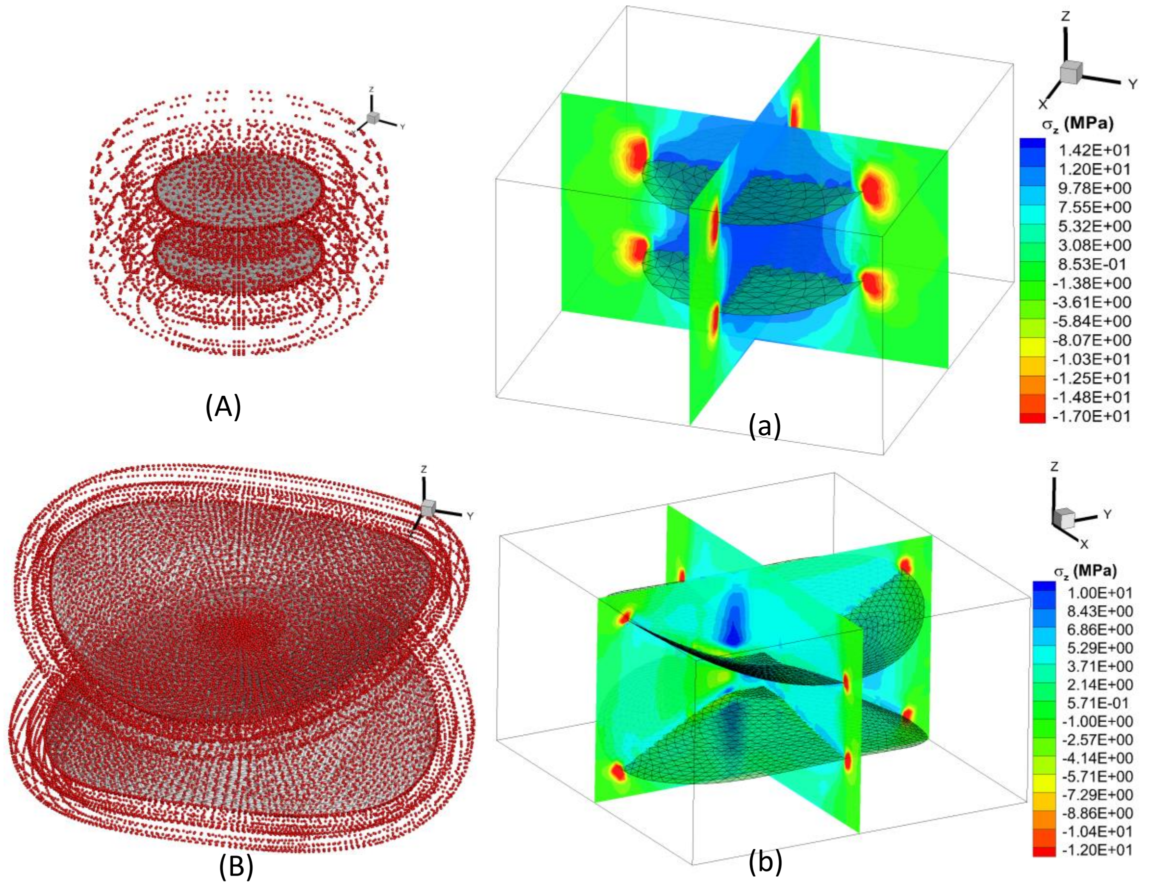

Figure 13. (A) and (B) are the sampled points for stress plots, and (a) and (b) are corresponding contours of stress variation, induced by the fracture, along the *z*-axis (the direction of original maximum principal stress): Example 2.

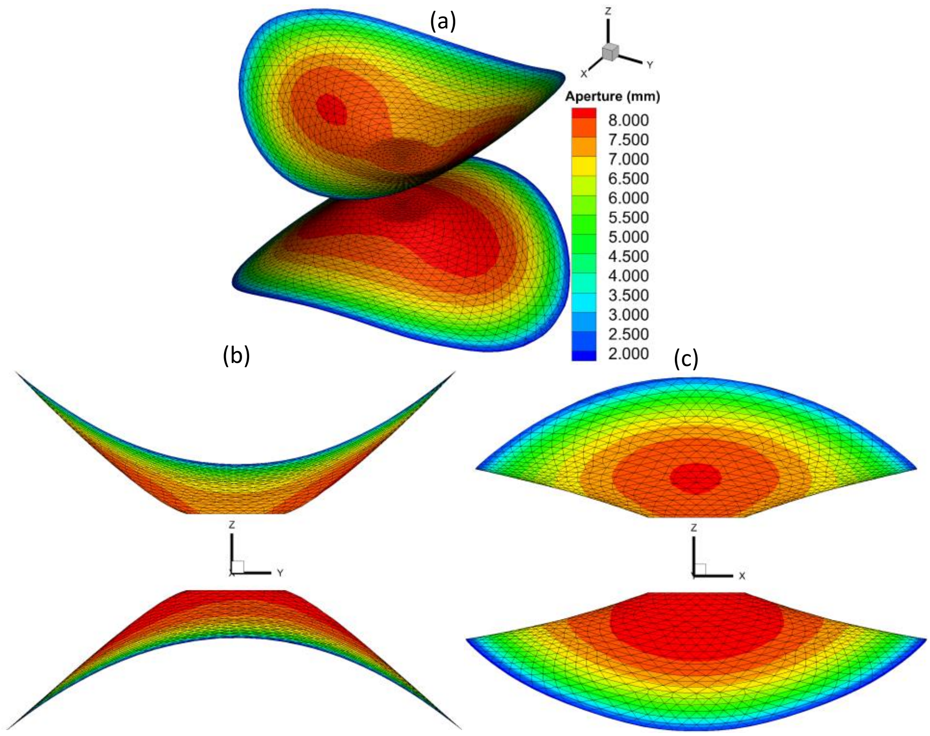

Figure 14. Geometries of the propagating nonplanar fractures and corresponding apertures after 25 advancement steps in 3-D side view: Example 2.

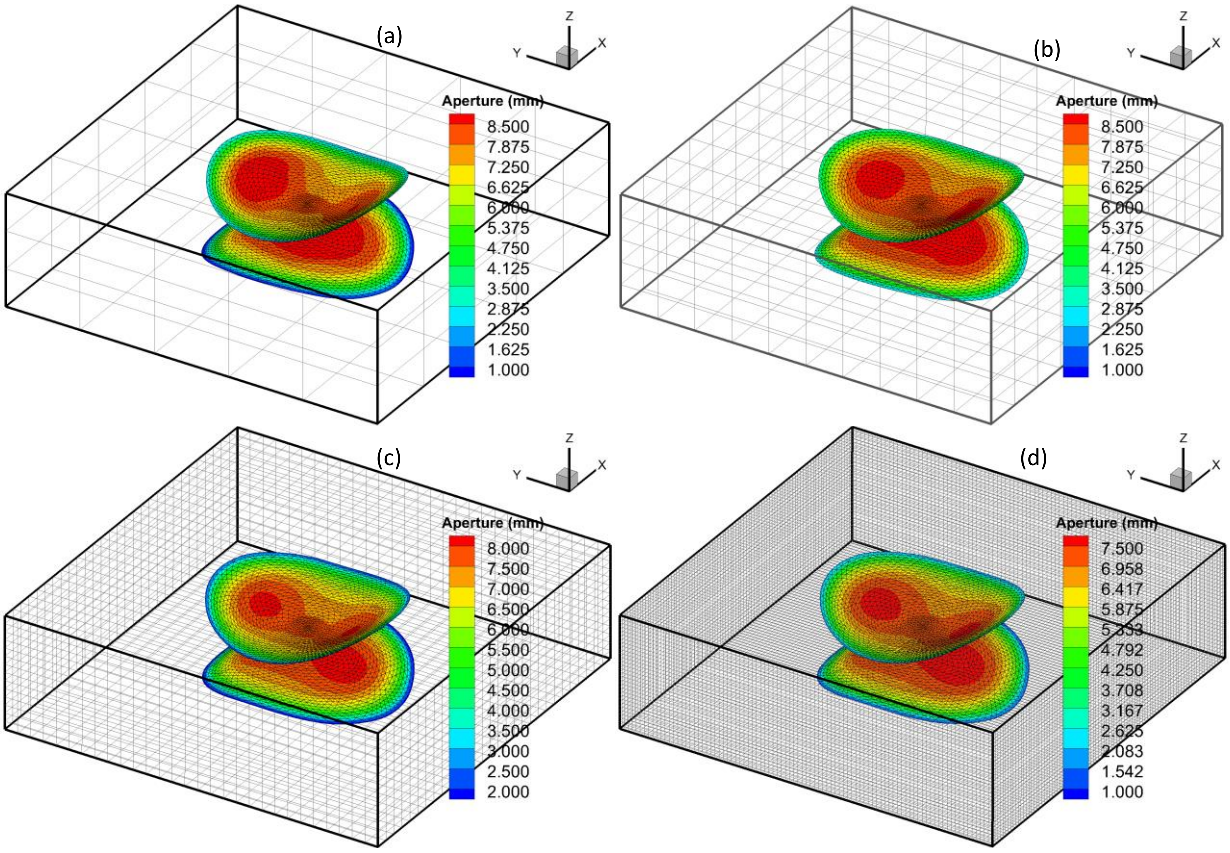

Figure 15. Fracture aperture distributions under various matrix grid resolutions: (a) $5 \times 5 \times 3$ grids; (b) $10 \times 10 \times 5$ grids; (c) $30 \times 30 \times 10$ grids; and (d) $90 \times 90 \times 30$ grids. Example 2.

6.3 Example 3: Propagation in Multiple En Échelon Fractures

En échelon fractures are commonly observed in geology, induced by a mechanical interaction between their near-tip stress fields [*Schultz*, 2019]. Figure 16 shows the multiscale feature of en échelon fractures, ranging from several centimeters (e.g., linked joint arrays, see panels b and c in Figure 16) to a few kilometers (e.g., overlapping en échelon faults, see Figure 16a). In this section, we will explore the simultaneous growth of multiple en échelon fractures with even spacing, driven by inner fluid pressure. As depicted in Figure 17, four radial fractures are evenly distributed in the domain with a dimension of $70\ \mathrm{m} \times 60\ \mathrm{m} \times 30\ \mathrm{m}$, which is divided into $29 \times 29 \times 14 = 11774$ identical matrix blocks. All of the fractures have the same geometric parameters, including fracture radius R=5.0 m, perpendicular spacing S=5.0 m, an overlap of inner tips D=4.0 m, and distance between fracture midpoints L=14.0 m. We assume that the fracturing is driven by the same fluid as used in Example 2 with a constant rate of Q=0.01 m^3/s. *In-situ* stress conditions and mechanical rock and fluid properties are the same as in Example 2.

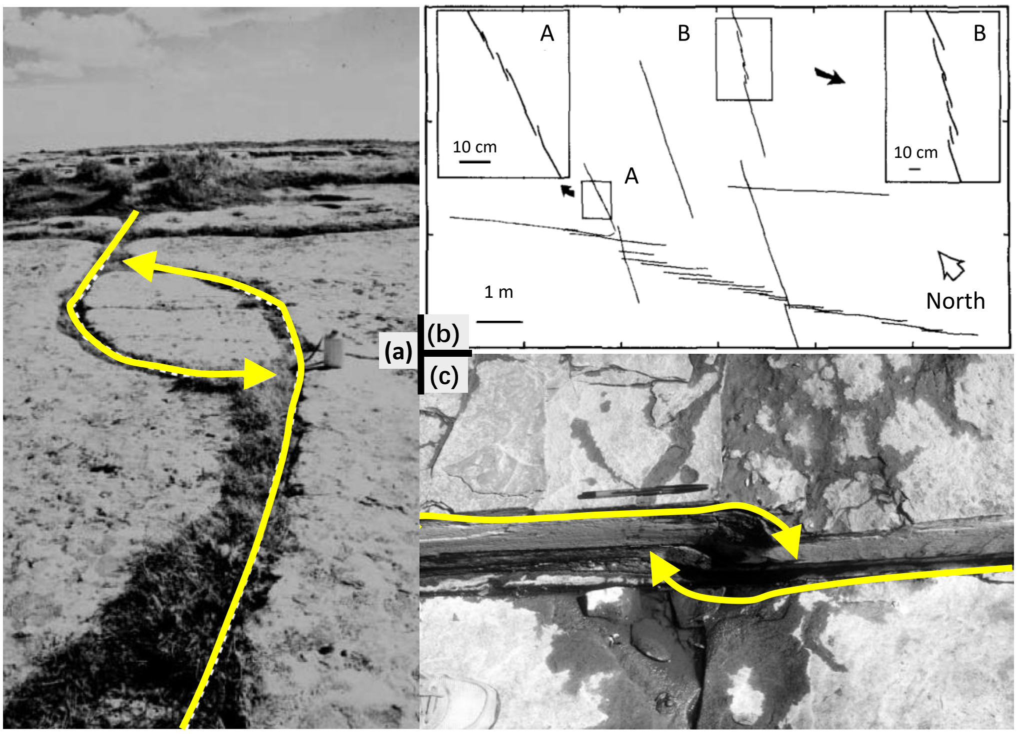

Figure 16. En échelon fractures: (a) mixed mode I-II curving pattern for overlapping en échelon fractures in sandstone, Oil Mountain, Wyoming [*Olson et al.*, 2009]; (b) joint traces mapped on bedding surface of Dakota Sandstone [*Olson and Pollard*, 1989]; and (c) a linked en échelon pair of joints [*Schultz*, 2019]: Example 3.

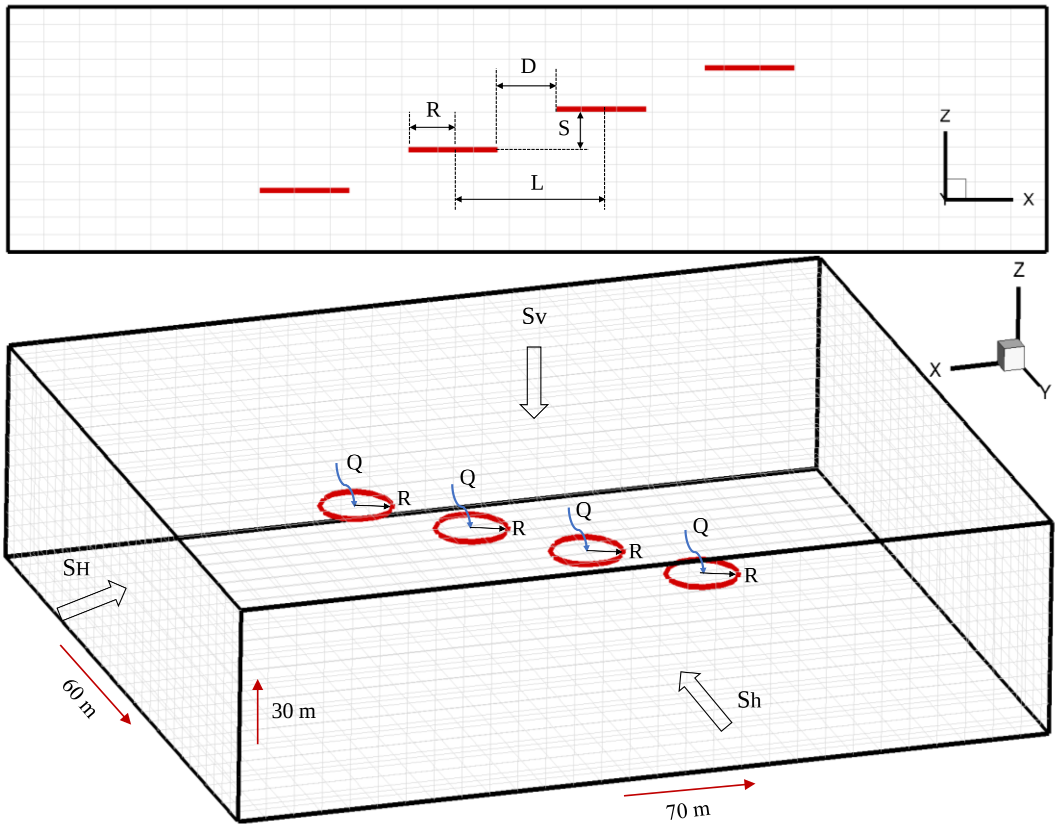

Figure 17. Illustration of the physical model for en échelon fractures' growth, driven by inner fluid pressure: Example 3.

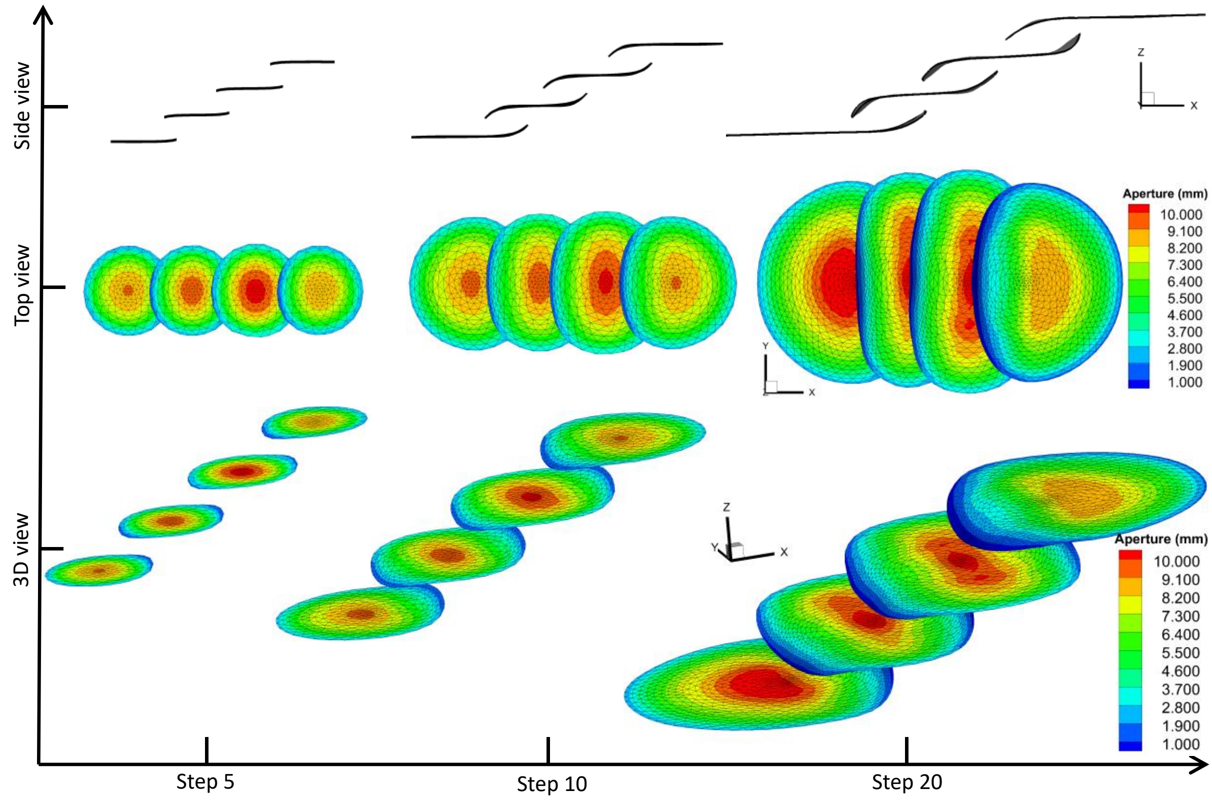

Figure 18. Geometries and aperture distributions of the propagating nonplanar fractures at different advancement steps in various views: Example 3.

Figure 18 shows the evolution of en échelon arrays at various propagation steps. Initially, each pair of the parallel, noncollinear fractures grow to approach each other (i.e., D>0), and all of the fractures exhibit a uniform growth rate. After two propagation steps (approximately 24 s), the tips become aligned, i.e., the overlap of inner tips is near zero. The mechanical interaction also becomes increasingly intense. The side views in Figure 18 display that the fractures grow past each other into an overlapped configuration, which is qualitatively similar to the results based on mapped data of joint traces (cf. Figure 16b). In subsequent growth steps, the fractures further grow toward each other and present roll-over configurations around the interacted fracture tips, as shown in the last panel of the side view in Figure 18 (also see Figure 16a and Figure 16c). The top view and 3-D view in Figure 18 show that the fracture growth is impeded after fractures' overlap since the magnitude of the front advancement sharply decreases within the overlapped region. On the other hand, the growth along the y-direction is enhanced and preferential propagation outward of the outer fractures can be observed. Enhancement or impediment of the growth ahead of an individual fracture front leads to asymmetric fracture geometry. Figure 19 shows the mechanical interaction among the en échelon arrays, in which the schematic diagrams for the sequential growth of en échelon arrays into underlapped, neutral, and overlapped configuration are slightly modified from *Schultz* [2019]. We present the stress contours corresponding to each case when the fractures are about to propagate. Results indicate that fracture-induced stresses alter the magnitude and the direction of the principal stress significantly, e.g., the increase or decrease of the stress along the *z*-axis is up to 10 MPa near the fractures. For the underlap configuration, the mechanical interaction between fractures is negligible such that the en échelon arrays propagate in pure mode I without change of direction. However, for neutral and overlapped cases, the stress shadowing effect will lead to a redistribution of the stress, resulting in fracture reorientation.

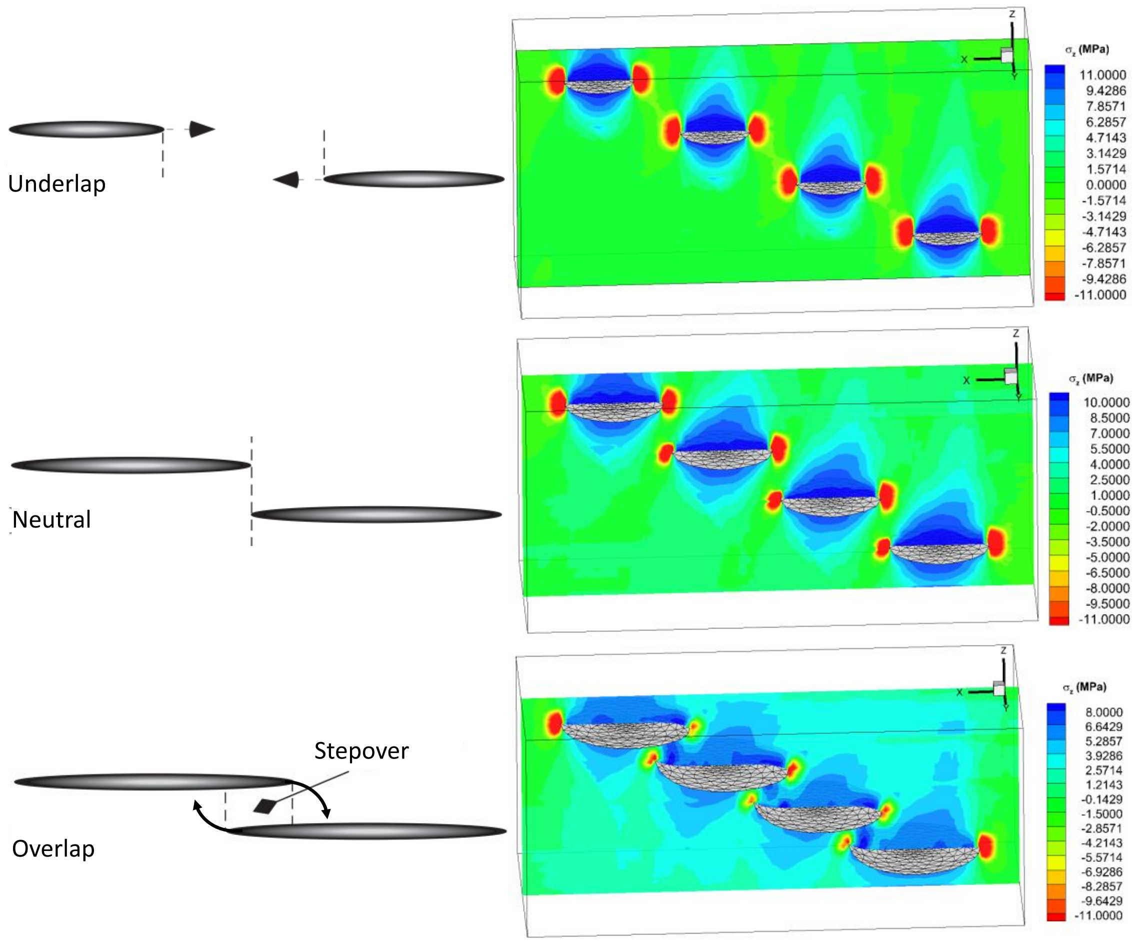

Figure 19. Sequential growth of en échelon fractures into underlapped, neutral, and overlapped configurations: the left panels are the schematic diagrams (after *Schultz* [2019]) and the right panels correspond to the stress contours along the z-direction after 0 step, 2 steps, and 10 steps, respectively: Example 3.

7. Summary

This paper describes a novel modeling framework for nonplanar 3-D fracture growth in poroelastic porous media, based on a hybrid numerical method. We validate the proposed model against asymptotic solutions for penny-shaped fracture propagation. To verify the simulation of nonplanar fracture propagation, numerical results are compared with the analytical solution of SIFs for an inclined radial fracture. Subsequently, we perform three numerical examples to explore planar and nonplanar fracture propagation. In Example 2, which covers planar fracture growth through three stress layers, the significance of stress contrast is confirmed for fracture containment. In examples 1 and 3, we explore the stress shadowing effect that causes redistribution of the stress field, leading to nonplanar 3-D fracture geometries. In Example 3, we find that the predicted configurations of en échelon arrays are consistent with the mapped data and the observed geological phenomena.

In this framework, the time-dependent fracture footprint is explicitly tracked by triangular grids, based on the BEM and the EDFM. The BEM is adopted to estimate the fracture aperture, fracture-induced stresses, as well as the fracture stiffness, and the EDFM is used to calculate fluid flow through the fractures and the fluid exchange between the matrix and the fracture. Our treatment possesses several distinct advantages. First, there is no need to refine the matrix grid for representing the fracture geometry, which often poses challenges to gridding and code development. Second, the leakoff is considered in fully 3-D, circumventing the limitations related to Carter's model. Third, all of the parameters for the fracture are physics-based, including the fracture geometry, fracture aperture, and the fluid pressure, such that the model can be readily extended to proppant transport and placement and the development of hydrocarbon/geothermal energy. To the best of our knowledge, we propose for the first time an iteratively coupled approach that is well-suited for fracture propagation simulation. This solution strategy makes the upscaling of coupled fluid flow, geomechanics, and fracture propagation viable because the 3-D BEM could render pressure-stress-scale-dependent fracture permeability and stiffness for flow and geomechanics.

Three are many important aspects that deserve further research in our future work. The model can be extended to account for preexisting natural fractures via incorporating 3-D crossing criteria between the natural and hydraulic fractures, and adjusting the grid system to describe the fracture intersection and merging (e.g., *Li and Zhang* [2019]; *Shi and Shen* [2018]). Another important topic, associated with the proposed model, is to integrate the proppant transport in complex fracture networks. Besides, the upscaling of geomechanics and fluid flow in fractured porous media is of high interest to hydrologists and petroleum engineers. Our future work will focus on how to utilize the 3-D BEM to form an effective homogenized technique from hydraulic and mechanical perspectives.

Acknowledgments

Sanbai Li expresses gratitude to Dr. Huiying Tang at Southwest Petroleum University for her valuable suggestions and discussions on this work. All of the data of numerical simulation results shown in this work are made available from a public repository of research data, Zenodo, through the following link: https://zenodo.org/record/3763410#.XqQ36f8zY2w.

References

Ambati, M., Gerasimov, T., & De Lorenzis, L. (2015). A review on phase-field models of brittle fracture and a new fast hybrid formulation, *Computational Mechanics*, *55*(2), 383-405. https://doi.org/10.1007/s00466-014-1109-y

Bandis, S., Lumsden, A., & Barton, N. (1983). Fundamentals of rock joint deformation, *International Journal of Rock Mechanics and Mining Sciences & Geomechanics Abstracts*, *20*(6), 249-268. https://doi.org/10.1016/0148-9062(83)90595-8

Belytschko, T., & Black, T. (1999). Elastic crack growth in finite elements with minimal remeshing, *International Journal for Numerical Methods in Engineering*, *45*(5), 601-620. https://doi.org/10.1002/(SICI)1097-0207(19990620)45:5<601::AID-NME598>3.0.CO;2-S

Brown, S. R. (1987). Fluid flow through rock joints: the effect of surface roughness, *Journal of Geophysical Research: Solid Earth*, *92*(B2), 1337-1347. https://doi.org/10.1029/JB092iB02p01337

Carter, E. D. (1957), Optimum fluid characteristics for fracture extension, paper presented at American Petroleum Institute Drilling and Production Practice, American Petroleum Institute.

Castonguay, S. T., Mear, M. E., Dean, R. H., & Schmidt, J. H. (2013), Predictions of the growth of multiple interacting hydraulic fractures in three dimensions, paper presented at SPE Annual Technical Conference and Exhibition, Society of Petroleum Engineers.

Cheng, W., Lu, C., & Zhou, Z. (2020). Modeling of borehole hydraulic fracture initiation and propagation with pre-existing cracks using the displacement discontinuity method, *Geotechnical and Geological Engineering*, 1-10. https://doi.org/10.1007/s10706-020-01195-8

Cherny, S., Lapin, V., Esipov, D., Kuranakov, D., Avdyushenko, A., Lyutov, A., et al. (2016). Simulating fully 3D non-planar evolution of hydraulic fractures, *International Journal of Fracture*, *201*(2), 181-211. https://doi.org/10.1007/s10704-016-0122-x

Cipolla, C. L., Warpinski, N. R., Mayerhofer, M., Lolon, E. P., & Vincent, M. (2010). The relationship between fracture complexity, reservoir properties, and fracture-treatment design, *SPE Production & Operations*, *25*(04), 438-452. https://doi.org/10.2118/115769-PA

Coussy, O. (2004). *Poromechanics*, John Wiley & Sons.

Crouch, S. L., Starfield, A. M., & Rizzo, F. (1983). Boundary element methods in solid mechanics, *Journal of Applied Mechanics*, *50*, 704. https://doi.org/10.1115/1.3167129

Cundall, P. A. (1971), A computer model for simulating progressive, large-scale movement in blocky rock system, paper presented at Proceedings of the International Symposium on Rock Mechanics, 1971.

Damjanac, B., & Cundall, P. (2016). Application of distinct element methods to simulation of hydraulic fracturing in naturally fractured reservoirs, *Computers and Geotechnics*, *71*, 283-294. https://doi.org/10.1016/j.compgeo.2015.06.007

Dittmann, M., Aldakheel, F., Schulte, J., Schmidt, F., Krüger, M., Wriggers, P., et al. (2019). Phase-field modeling of porous-ductile fracture in non-linear thermo-elasto-plastic solids, *Computer Methods in Applied Mechanics and*

Engineering, 112730. https://doi.org/10.1016/j.cma.2019.112730
Dontsov, E., & Peirce, A. (2017). A multiscale implicit level set algorithm (ILSA) to model hydraulic fracture propagation incorporating combined viscous, toughness, and leak-off asymptotics, *Computer Methods in Applied Mechanics and Engineering*, *313*, 53-84. https://doi.org/10.1016/j.cma.2016.09.017
Duarte, C. A., Hamzeh, O., Liszka, T., & Tworzydlo, W. (2001). A generalized finite element method for the simulation of three-dimensional dynamic crack propagation, *Computer Methods in Applied Mechanics and Engineering*, *190*(15-17), 2227-2262. https://doi.org/10.1016/S0045-7825(00)00233-4
Duarte, C. A., Reno, L., & Simone, A. (2007). A high-order generalized FEM for through-the-thickness branched cracks, *International Journal for Numerical Methods in Engineering*, *72*(3), 325-351. https://doi.org/10.1002/nme.2012
Fan, H., Li, S., Feng, X.-T., & Zhu, X. (2020). A high-efficiency 3D boundary element method for estimating the stress/displacement field induced by complex fracture networks, *Journal of Petroleum Science and Engineering*, *187*, 106815. https://doi.org/10.1016/j.petrol.2019.106815
Fisher, M. K., & Warpinski, N. R. (2012). Hydraulic-fracture-height growth: Real data, *SPE Production & Operations*, *27*(01), 8-19. https://doi.org/10.2118/145949-PA
Fu, P., Settgast, R. R., Hao, Y., Morris, J. P., & Ryerson, F. J. (2017). The influence of hydraulic fracturing on carbon storage performance, *Journal of Geophysical Research: Solid Earth*, *122*(12), 9931-9949. https://doi.org/10.1002/2017JB014942
Gordeliy, E., & Peirce, A. (2013). Coupling schemes for modeling hydraulic fracture propagation using the XFEM, *Computer Methods in Applied Mechanics and Engineering*, *253*, 305-322. https://doi.org/10.1016/j.cma.2012.08.017
Gordeliy, E., & Peirce, A. (2015). Enrichment strategies and convergence properties of the XFEM for hydraulic fracture problems, *Computer Methods in Applied Mechanics and Engineering*, *283*, 474-502. https://doi.org/10.1016/j.cma.2014.09.004
Gupta, P., & Duarte, C. A. (2014). Simulation of non-planar three-dimensional hydraulic fracture propagation, *International Journal for Numerical and Analytical Methods in Geomechanics*, *38*(13), 1397-1430. https://doi.org/10.1002/nag.2305
Gupta, P., & Duarte, C. A. (2018). Coupled hydromechanical-fracture simulations of nonplanar three-dimensional hydraulic fracture propagation, *International Journal for Numerical and Analytical Methods in Geomechanics*, *42*(1), 143-180. https://doi.org/10.1002/nag.2719
Gupta, V., Kim, D.-J., & Duarte, C. A. (2012). Analysis and improvements of global-local enrichments for the generalized finite element method, *Computer Methods in Applied Mechanics and Engineering*, *245*, 47-62. https://doi.org/10.1016/j.cma.2012.06.021
Hamidi, F., & Mortazavi, A. (2014). A new three dimensional approach to numerically model hydraulic fracturing process, *Journal of Petroleum Science and Engineering*, *124*, 451-467. https://doi.org/10.1016/j.petrol.2013.12.006
Hou, B., Chen, M., Cheng, W., & Diao, C. (2016). Investigation of hydraulic fracture networks in shale gas reservoirs with random fractures, *Arabian Journal for Science and Engineering*, *41*(7), 2681-2691. https://doi.org/10.1007/s13369-015-1829-0
Izadi, G., & Elsworth, D. (2014). Reservoir stimulation and induced seismicity: Roles of fluid pressure and thermal transients on reactivated fractured networks, *Geothermics*, *51*, 368-379. https://doi.org/10.1016/j.geothermics.2014.01.014
Ji, L., Settari, A., & Sullivan, R. B. (2009). A novel hydraulic fracturing model fully coupled with geomechanics and reservoir simulation, *SPE Journal*, *14*(03), 423-430. https://doi.org/10.2118/110845-PA
Kassir, M. K., & Sih, G. C. (1975). *Mechanics of fracture 2: Three-dimensional crack problems*, Leyden: Noordhoff

International Publishing.

Kim, J., & Moridis, G. J. (2015). Numerical analysis of fracture propagation during hydraulic fracturing operations in shale gas systems, *International Journal of Rock Mechanics and Mining Sciences*, *76*, 127-137. https://doi.org/10.1016/j.ijrmms.2015.02.013

Kresse, O., Weng, X., Gu, H., & Wu, R. (2013). Numerical modeling of hydraulic fractures interaction in complex naturally fractured formations, *Rock Mechanics and Rock Engineering*, *46*(3), 555-568. https://doi.org/10.1007/s00603-012-0359-2

Krysl, P., & Belytschko, T. (1999). The element free Galerkin method for dynamic propagation of arbitrary 3-D cracks, *International Journal for Numerical Methods in Engineering*, *44*(6), 767-800. https://doi.org/10.1002/(SICI)1097-0207(19990228)44:6<767::AID-NME524>3.0.CO;2-G

Kumar, D., & Ghassemi, A. (2018). Three-dimensional poroelastic modeling of multiple hydraulic fracture propagation from horizontal wells, *International Journal of Rock Mechanics and Mining Sciences*, *105*, 192-209. https://doi.org/10.1016/j.ijrmms.2018.01.010

Kuriyama, K., & Mizuta, Y. (1993). Three-dimensional elastic analysis by the displacement discontinuity method with boundary division into triangular leaf elements, *International Journal of Rock Mechanics and Mining Sciences & Geomechanics Abstracts*, *30*(2), 111-123. https://doi.org/10.1016/0148-9062(93)90704-H

Lecampion, B., Bunger, A., & Zhang, X. (2018). Numerical methods for hydraulic fracture propagation: a review of recent trends, *Journal of Natural Gas Science and Engineering*, *49*, 66-83. https://doi.org/10.1016/j.jngse.2017.10.012

Lee, S., Wheeler, M. F., & Wick, T. (2016). Pressure and fluid-driven fracture propagation in porous media using an adaptive finite element phase field model, *Computer Methods in Applied Mechanics and Engineering*, *305*, 111-132. https://doi.org/10.1016/j.cma.2016.02.037

Li, L., & Lee, S. H. (2008). Efficient field-scale simulation of black oil in a naturally fractured reservoir through discrete fracture networks and homogenized media, *SPE Reservoir Evaluation & Engineering*, *11*(04), 750-758. https://doi.org/10.2118/103901-PA

Li, S., Feng, X.-T., Zhang, D., & Tang, H. (2019). Coupled thermo-hydro-mechanical analysis of stimulation and production for fractured geothermal reservoirs, *Applied Energy*, *247*, 40-59. https://doi.org/10.1016/j.apenergy.2019.04.036

Li, S., Kang, Z., Feng, X.-T., Pan, Z., Huang, X., & Zhang, D. (2020). Three-dimensional hydrochemical model for dissolutional growth of fractures in karst aquifers, *Water Resources Research*, *56*(3). https://doi.org/10.1029/2019WR025631

Li, S., Li, X., & Zhang, D. (2016). A fully coupled thermo-hydro-mechanical, three-dimensional model for hydraulic stimulation treatments, *Journal of Natural Gas Science and Engineering*, *34*, 64-84. https://doi.org/10.1016/j.jngse.2016.06.046

Li, S., & Zhang, D. (2018). A fully coupled model for hydraulic-fracture growth during multiwell-fracturing treatments: enhancing fracture complexity, *SPE Production & Operations*, *33*(02), 235-250. https://doi.org/10.2118/182674-PA

Li, S., & Zhang, D. (2019). How effective is carbon dioxide as an alternative fracturing fluid?, *SPE Journal*, *24*(02), 857-876. https://doi.org/10.2118/194198-PA

Li, X., Zhang, D., & Li, S. (2015). A multi-continuum multiple flow mechanism simulator for unconventional oil and gas recovery, *Journal of Natural Gas Science and Engineering*, *26*, 652-669. https://doi.org/10.1016/j.jngse.2015.07.005

Miehe, C., Schaenzel, L.-M., & Ulmer, H. (2015). Phase field modeling of fracture in multi-physics problems. Part I. Balance of crack surface and failure criteria for brittle crack propagation in thermo-elastic solids, *Computer*

Methods in Applied Mechanics and Engineering, *294*, 449-485. https://doi.org/10.1016/j.cma.2014.11.016

Moës, N., Dolbow, J., & Belytschko, T. (1999). A finite element method for crack growth without remeshing, *International Journal for Numerical Methods in Engineering*, *46*(1), 131-150. https://doi.org/10.1002/(SICI)1097-0207(19990910)46:1<131::AID-NME726>3.0.CO;2-J

Mohammadnejad, T., & Andrade, J. (2016). Numerical modeling of hydraulic fracture propagation, closure and reopening using XFEM with application to in-situ stress estimation, *International Journal for Numerical and Analytical Methods in Geomechanics*, *40*(15), 2033-2060. https://doi.org/10.1002/nag.2512

Nagel, N., Sanchez-Nagel, M., Zhang, F., Garcia, X., & Lee, B. (2013). Coupled numerical evaluations of the geomechanical interactions between a hydraulic fracture stimulation and a natural fracture system in shale formations, *Rock Mechanics and Rock Engineering*, *46*(3), 581-609. https://doi.org/10.1007/s00603-013-0391-x

Olson, J., & Pollard, D. D. (1989). Inferring paleostresses from natural fracture patterns: A new method, *Geology*, *17*(4), 345-348. https://doi.org/10.1130/0091-7613(1989)017<0345:IPFNFP>2.3.CO;2

Olson, J. E. (2004). Predicting fracture swarms—The influence of subcritical crack growth and the crack-tip process zone on joint spacing in rock, *Geological Society, London, Special Publications*, *231*(1), 73-88. https://doi.org/10.1144/GSL.SP.2004.231.01.05

Olson, J. E., Laubach, S. E., & Lander, R. H. (2009). Natural fracture characterization in tight gas sandstones: Integrating mechanics and diagenesis, *AAPG Bulletin*, *93*(11), 1535-1549. https://doi.org/10.1306/08110909100

Olson, J. E., & Taleghani, A. D. (2009), Modeling simultaneous growth of multiple hydraulic fractures and their interaction with natural fractures, paper presented at SPE Hydraulic Fracturing Technology Conference, Society of Petroleum Engineers.

Paul, B., Faivre, M., Massin, P., Giot, R., Colombo, D., Golfier, F., et al. (2018). 3D coupled HM-XFEM modeling with cohesive zone model and applications to non planar hydraulic fracture propagation and multiple hydraulic fractures interference, *Computer Methods in Applied Mechanics and Engineering*, *342*, 321-353. https://doi.org/10.1016/j.cma.2018.08.009

Pereira, J., Duarte, C. A., Guoy, D., & Jiao, X. (2009). hp-Generalized FEM and crack surface representation for non-planar 3-D cracks, *International Journal for Numerical Methods in Engineering*, *77*(5), 601-633. https://doi.org/10.1002/nme.2419

Permann, C. J., Tonks, M. R., Fromm, B., & Gaston, D. R. (2016). Order parameter re-mapping algorithm for 3D phase field model of grain growth using FEM, *Computational Materials Science*, *115*, 18-25. https://doi.org/10.1016/j.commatsci.2015.12.042

Salimzadeh, S., Paluszny, A., & Zimmerman, R. W. (2017). Three-dimensional poroelastic effects during hydraulic fracturing in permeable rocks, *International Journal of Solids and Structures*, *108*, 153-163. https://doi.org/10.1016/j.ijsolstr.2016.12.008

Savitski, A., & Detournay, E. (2002). Propagation of a penny-shaped fluid-driven fracture in an impermeable rock: asymptotic solutions, *International Journal of Solids and Structures*, *39*(26), 6311-6337. https://doi.org/10.1016/S0020-7683(02)00492-4

Schöllmann, M., Richard, H. A., Kullmer, G., & Fulland, M. (2002). A new criterion for the prediction of crack development in multiaxially loaded structures, *International Journal of Fracture*, *117*(2), 129-141. https://doi.org/10.1023/A:1020980311611

Schultz, R. A. (2019). Discontinuity patterns and their interpretation, in *Geologic Fracture Mechanics*, edited, pp. 170-208, Cambridge University Press, Cambridge 10.1017/9781316996737.005

Shen, B., & Shi, J. (2019). A numerical scheme of coupling of fluid flow with three-dimensional fracture propagation, *Engineering Analysis with Boundary Elements*, *106*, 243-251. https://doi.org/10.1016/j.enganabound.2019.05.017

Shi, J., & Shen, B. (2018). Simulation implementation of trajectory and intersections of three-dimensional crack growths with displacement discontinuity method, *Engineering Fracture Mechanics*, *204*, 119-137. https://doi.org/10.1016/j.engfracmech.2018.10.008

Sokolnikoff, I. S., & Specht, R. D. (1956). *Mathematical theory of elasticity*, McGraw-Hill New York.

Tang, H., Wang, S., Zhang, R., Li, S., Zhang, L., & Wu, Y.-S. (2019). Analysis of stress interference among multiple hydraulic fractures using a fully three-dimensional displacement discontinuity method, *Journal of Petroleum Science and Engineering*, *179*, 378-393. https://doi.org/10.1016/j.petrol.2019.04.050

Tang, H., Winterfeld, P. H., Wu, Y.-S., Huang, Z.-q., Di, Y., Pan, Z., et al. (2016). Integrated simulation of multi-stage hydraulic fracturing in unconventional reservoirs, *Journal of Natural Gas Science and Engineering*, *36*, 875-892. https://doi.org/10.1016/j.jngse.2016.11.018

Thomas, R. N., Paluszny, A., & Zimmerman, R. W. (2017). Quantification of fracture interaction using stress intensity factor variation maps, *Journal of Geophysical Research: Solid Earth*, *122*(10), 7698-7717. https://doi.org/10.1002/2017JB014234

Thomas, R. N., Paluszny, A., & Zimmerman, R. W. (2020a). Growth of three-dimensional fractures, arrays, and networks in brittle rocks under tension and compression, *Computers and Geotechnics*, *121*, 103447. https://doi.org/10.1016/j.compgeo.2020.103447

Thomas, R. N., Paluszny, A., & Zimmerman, R. W. (2020b). Permeability of three-dimensional numerically grown geomechanical discrete fracture networks with evolving geometry and mechanical apertures, *Journal of Geophysical Research: Solid Earth*. https://doi.org/10.1029/2019JB018899

Weng, X., Kresse, O., Cohen, C. E., Wu, R., & Gu, H. (2011), Modeling of hydraulic fracture network propagation in a naturally fractured formation, paper presented at SPE Hydraulic Fracturing Technology Conference, Society of Petroleum Engineers.

Wick, T., Singh, G., & Wheeler, M. F. (2016). Fluid-filled fracture propagation with a phase-field approach and coupling to a reservoir simulator, *SPE Journal*, *21*(03), 981-999. https://doi.org/10.2118/168597-PA

Wilson, Z. A., & Landis, C. M. (2016). Phase-field modeling of hydraulic fracture, *Journal of the Mechanics and Physics of Solids*, *96*, 264-290. https://doi.org/10.1016/j.jmps.2016.07.019

Xu, Y., Cavalcante Filho, J. S., Yu, W., & Sepehrnoori, K. (2017). Discrete-fracture modeling of complex hydraulic-fracture geometries in reservoir simulators, *SPE Reservoir Evaluation & Engineering*, *20*(02), 403-422. https://doi.org/10.2118/183647-PA

Yao, M., Chang, H., Li, X., & Zhang, D. (2018). Tuning fractures with dynamic data, *Water Resources Research*, *54*(2), 680-707. https://doi.org/10.1002/2017WR022019

Yoon, J. S., Zimmermann, G., & Zang, A. (2015). Numerical investigation on stress shadowing in fluid injection-induced fracture propagation in naturally fractured geothermal reservoirs, *Rock Mechanics and Rock Engineering*, *48*(4), 1439-1454. https://doi.org/10.1007/s00603-014-0695-5

Zhang, X., Wu, B., Jeffrey, R. G., Connell, L. D., & Zhang, G. (2017). A pseudo-3D model for hydraulic fracture growth in a layered rock, *International Journal of Solids and Structures*, *115*, 208-223. https://doi.org/10.1016/j.ijsolstr.2017.03.022

Zidane, A., & Firoozabadi, A. (2020). Higher-order simulation of two-phase compositional flow in 3D with non-planar fractures, *Journal of Computational Physics*, *402*, 108896. https://doi.org/10.1016/j.jcp.2019.108896